POLITECNICO DI TORINO

Collegio di Ingegneria Chimica e dei Materiali

Master of Science Course
in Materials Engineering

Master of Science Thesis

Comparison between the surface roughness and mechanical properties of AISI 316L samples produced via Laser Power Bed Fusion process using gas atomized and water atomized powders

Tutors

prof. Luca Iuliano
prof. Abdollah Saboori

Candidate

Niccolò Zapparoli

October 2021

Abstract

Laser powder bed fusion (LPBF) is an additive manufacturing technology that allows the production of the component with complex geometry and excellent mechanical properties. Many process variables are investigated to reach a better comprehension and control of the process. This thesis work focuses on a specific feature of the LPBF process, the feedstock material. The attention is on a particular material, AISI 316L stainless steel. The powder used as feedstock material can be produced via gas atomizing (GA) or water atomizing (WA) and can influence the process and the product in a significant way. For this reason, the first part of this work is a literature review on how the powder affects the process. Subsequently, the relationship between the type of powder and the properties of the built part is considered. In the second part of this thesis, experimental research is carried out. The work starts with producing two sets of cubic samples with different sets of process parameters. The first set uses GA powder as feedstock material, while the second uses WA powder. The parts produced are then used for the testing of dimensional accuracy, density, and surface roughness. After the selection of the optimal set of process parameters, tensile samples are produced and tested. All the results achieved are then compared to investigate the effect of the two types of powder. As a result of the comparison, the GA powder allows the production of denser and more homogeneous powder bed and, consequently, reach a higher density of as-built samples. The yield strength achieved is slightly lower in the case of WA powder, while the elongation at break is much more excellent in GA samples.

Index

1. Riassunto in italiano 1

2. Introduction 11

3. State of art 15

    3.1 Feedstock material 15

    3.2 Process parameters optimization 16

    3.3 Microstructure 17

    3.4 Mechanical properties 19

        3.4.1 Fracture surface 23

    3.5 Surface roughness 26

    3.6 Cost analysis 26

4. Material and methods 29

    4.1 Feedstock material 29

    4.2 Design of Experiment 29

    4.3 Testing methods 32

5. Results and discussion 35

    5.1 Dimensional accuracy 35

    5.2 Density 35

    5.3 Surface roughness 38

    5.4 Mechanical properties 40

6. Conclusions 43

7. Bibliography 45

8. List of acronyms 53

9. List of symbols 55

Appendix I 57

Appendix II 59

Appendix III 61

1. Riassunto in italiano

Introduzione

Il lavoro svolto in questa tesi riguarda lo studio dell'effetto di due differenti tipi di polvere utilizzata come materiale di partenza per un processo di manifattura additiva, in particolare il processo LPBF (Laser Powder Bed Fusion). L'obiettivo del lavoro è quello di produrre un confronto riguardante il tipo di materia prima utilizzata che possa riempire un vuoto presente in letteratura scientifica. Il lavoro è diviso in cinque sezioni, dopo una breve introduzione, viene condotta una ricerca dello stato dell'arte della tecnologia. Nella terza parte viene discussa la produzione e l'analisi dei campioni. Successivamente, nella quarta sezione vengono dichiarati e commentati i risultati. Nell'ultima parte invece vengono discusse le conclusioni generali.

Le tecniche di manifattura additiva hanno attratto l'interesse di ricercatori e aziende grazie alle peculiarità del processo. Infatti, è possibile ottenere componenti con geometrie complesse in maniera più semplice rispetto a metodi tradizionali. La libertà di progettazione può altresì permettere la produzione di componenti con geometrie ottimizzate per la riduzione della massa. La produzione parte da un modello CAD, il quale viene sezionato in strati. Gli strati ottenuti sono quindi prodotti successivamente tramite la fusione e successiva solidificazione di un materiale di apporto (polvere o filo) tramite una sorgente di calore (laser, fascio elettronico o arco elettrico) guidata dal macchinario.

I processi di manifattura additiva per i metalli possono essere divisi in due grandi gruppi, i sistemi a letto di polvere (*PBF, Powder Bed Fusion*) e sistemi a deposizione diretta di energia (*DED, Directed Energy Deposition*). I sistemi a letto di polvere possono essere distinti sulla base della fonte di calore, che può essere un laser (LPBF), oppure un fascio elettronico (*EBM, Electron Beam Melting*). In entrambi i casi il letto di polvere viene formato con l'ausilio di una racla che posiziona la polvere. Le tecniche DED non includono un letto di polvere ma il materiale viene fornito da una testa di deposizione attraverso la quale viene fornito anche il calore necessario. Le tre principali tecnologie hanno caratteristiche differenti, ad esempio lo spessore di ogni strato può variare dai 20 – 50 µm per LPBF, 50 – 250 µm per l'EBM, fino ad arrivare ai 600 µm ottenibili con la DED. La velocità di produzione è un punto debole per la tecnica EBM a causa della necessità di trattamenti successivi alla solidificazione del componente prodotto. La DED riesce ad ottenere una miglior velocità di produzione rispetto al LPBF. Anche il materiale deve rispettare determinate condizioni per ogni processo, infatti la polvere usata per l'EBM ha granulometria compresa tra 45 – 105 µm, per il LPBF la polvere deve essere più fine di 50 µm, mentre la DED ha un materiale più grossolano, fino a 150 µm.

Nella Tabella 2.1 sono riportati diversi nomi commerciali per il processo LPBF. Il processo è schematizzato in Figura 2.1. Inizialmente, la polvere viene distribuita a formare il letto di polvere, il cui spessore viene selezionato in fase di progetto. Successivamente il laser scansiona la sezione prescritta dal file CAD. Infine la piattaforma viene abbassata e il ciclo può ripetersi fino al completamento del componente.

Le variabili all'interno del processo sono numerose e un loro controllo e ottimizzazione permette la produzione di un componente con qualità ottimali, come ad esempio densità, proprietà meccaniche o accuratezza dimensionale. Gusarov et al. [24] hanno diviso i parametri di processo in tre gruppi. Il primo è legato alla sorgente di energia, il secondo alle condizioni ambientali e il terzo al materiale. In questo lavoro l'analisi è focalizzata su alcuni parametri, ad esempio la potenza del laser (*laser power*), la velocità di scansione (*scanning speed*), lo spazio tra il centro di una traccia e quello adiacente (*hatch spacing*) e lo spessore dello strato (*layer thickness*).

Gli acciai inossidabili attraggono interesse a causa della loro capacità di resistere ad ambienti aggressivi e alle ottime proprietà meccaniche. Il comportamento in ambienti erosivi è un ulteriore forza di questa classe di acciai che li rende adatti a svariate applicazioni [26]. L'acciaio AISI 316L è uno dei maggiormente studiati e utilizzati.

Unendo le caratteristiche di questo materiale e del processo LPBF si possono ottenere componenti con ottime caratteristiche meccaniche, elevata complessità geometrica e massa ridotta.

Stato dell'arte

Il materiale sotto forma di polvere utilizzato ha generalmente una granulometria minore di 65 µm. La formazione del letto di polvere influisce su tutto il processo successivo, per questa ragione numerosi studi indagano le proprietà delle polveri. Due fattori hanno un ruolo rilevante, il primo è la scorrevolezza delle polveri. Infatti, polveri facilmente distribuibili formano un letto più omogeneo, varie caratteristiche delle polveri possono influenzare la loro scorrevolezza. In primis, la forma, polveri sferiche oppongono meno resistenza al moto. In aggiunta, una bassa rugosità superficiale favorisce lo scorrimento. Infine, le polveri fini, possedendo una maggiore superficie specifica, sono soggette ad attrazione di tipo Van der Waals. Il secondo aspetto fondamentale per ottenere un letto di polvere con caratteristiche ottimali è la capacità delle polveri di compattarsi, polveri sferiche riescono a riempire in modo più efficace lo spazio rispetto a polveri con forme irregolari.

Le polveri possono essere ottenute attraverso diversi processi di atomizzazione, tramite gas (GA), acqua (WA) o plasma (PA). Le differenze nei processi si ripercuotono sulla forma della particella, infatti, a causa dell'elevato gradiente termico le polveri GA hanno forma sferica, visibile in Figura 3.1a, elevata sfericità è raggiunta anche dalle polveri prodotte con PA. Le polveri WA invece hanno una forma irregolare, come mostrato in Figura 3.1b. Anche la composizione chimica varia in base al processo. Il lento e controllato processo PA non introduce impurità ma ha costi elevati. Il processo WA è molto economico ma introduce elevati tenori di ossigeno. Le polveri GA hanno un modesto contenuto di ossigeno e una forma sferica. Queste caratteristiche, insieme al costo minore rispetto alle polveri PA, rendono queste polveri il miglior compromesso per la tecnica LPBF.

L'ossigeno introdotto nelle polveri può produrre un infragilimento del componente e un calo delle proprietà meccaniche. In alcuni casi queste impurità possono portare ad un aumento delle proprietà meccaniche. Il contenuto di manganese è generalmente minore nelle polveri WA per ridurre il rischio di formazione di ossidi, favorita dalla maggiore presenza di ossigeno. Nel processo LPBF è possibile il riciclo delle polveri che non vengono interessate dalla fusione. Le polveri riciclate hanno una dimensione maggiore rispetto alle polveri vergini, inoltre il contenuto di ossigeno è leggermente maggiore.

I numerosi parametri di processo devono essere ottimizzati per ottenere un componente che abbia una densità il più vicino possibile a quella teorica. L'ottimizzazione è un processo sperimentale in cui vengono utilizzati diversi set di parametri di processo per la produzione di provini che vengono successivamente analizzati. In molti lavori viene considerato un parametro detto densità volumetrica di energia che include altri parametri come riportato nell'Equazione 3.1. Come mostrato in Figura 3.2 i campioni prodotti aumentano la loro densità all'aumentare della VED. Per bassi valori di VED si ha una mancata fusione, mentre per valori eccessivamente alti di VED si notano porosità dovute a gas prodotto dalla locale ebollizione del materiale.

Analizzando nello specifico i differenti parametri di processo che concorrono a definire la VED si evidenziano differenti effetti delle variabili di processo sulla densità. Il primo parametro che si considera è la potenza del laser. Si nota come, mantenendo costante la VED, un incremento della potenza comporti un innalzamento della densità del prodotto. Come riportato da Deng et al. [48], la tendenza viene mantenuta fino a quando non si raggiungono livelli elevati di potenza tali da provocare difetti nella struttura. Il secondo parametro analizzato è l'*hatch spacing*, è importante notare come questo parametro possa variare in un intervallo limitato. Infatti, una distanza troppo grande non permette la formazione di una struttura coesa a causa di porosità dovute alla

mancanza di fusione delle polveri, mentre una distanza troppo piccola comporta problemi di sovra-riscaldamento. Le variazioni di *hatch spacing* sono considerate ad un valore di VED costante, modificando di conseguenza la velocità di scansione. Dong et al. [49] riportano come il range ottimale di variazione dell'*hatch spacing* ricada tra i 75 e 100 μm. L'ultimo parametro è lo spessore del singolo strato, in generale i risultati riportano come all'aumentare dello spessore si abbia una diminuzione della densità a causa della difficoltà di penetrazione del calore. In alcuni casi, invece, si arriva a spessori fino a 250 μm.

La microstruttura influisce sulle proprietà del componente finito, i prodotti del processo LPBF mostrano delle strutture differenti rispetto ai metodi tradizionali di produzione. La dimensione dei grani dei prodotti della manifattura additiva è minore rispetto ai componenti prodotti con metodi convenzionali. La ragione di questa differenza risiede nella rapidità del processo LPBF, infatti, il calore viene fornito e dissipato in intervalli di tempo molto ristretti, di conseguenza la solidificazione è rapida e il grano rimane fine. Una tipica struttura presente è la *melt pool*, tramite un microscopio ottico si notano forme semi-circolari sovrapposte, esse sono il segno delle successive scansioni ad opera del laser. La *melt pool* è più profonda del singolo strato in quanto viene fusa una porzione maggiore per poter avere coesione tra i diversi strati. I grani presenti hanno una forma allungata che segue la direzione del flusso termico, inoltre i grani si estendono oltre i limiti della *melt pool*, simbolo di crescita epitassiale. Nonostante i metodi convenzionali producano componenti con una parziale presenza di martensite (circa 3%), il processo LPBF in molti casi produce una microstruttura composta da un'unica fase austenitica. In alcuni lavori è stata rilevata la presenza di altre fasi, come ad esempio ferrite [50]. Tramite l'analisi XRD si è visto come la struttura cristallina sia differente se si comparano le polveri e il prodotto finale, in quanto si ha un ampiamento dei picchi a causa delle irregolarità nella struttura cristallina introdotte dagli stress termici. Un comune difetto della microstruttura è il *balling*, riportato in Figura 3.5. Il fenomeno del *balling* si mostra con la presenza di particelle non fuse o parzialmente fuse. Le cause sono da ricercare nell'eccessivo calore fornito al materiale, il quale modifica la sua bagnabilità e non perfette la corretta fusione [60]; un'altra ragione è l'insufficiente energia fornita che non permette la fusione di tutte le polveri [59].

Uno degli aspetti fondamentali che vengono considerati per valutare la qualità del processo sono le proprietà meccaniche. È quindi doveroso confrontare le proprietà meccaniche di componenti prodotti con metodi convenzionali con i processi di manifattura additiva, come riportato nella Tabella 3.1. La maggiore differenza si può notare nella resistenza a snervamento. Le migliori proprietà meccaniche ottenute con il processo LPBF rispetto ai metodi tradizionali è sicuramente un vantaggio per la manifattura additiva. La differenza nei valori ottenuti ha origine nella differente velocità raffreddamento, ampiamente maggiore nel caso del processo LPBF. La diversa storia termica del materiale influenza la granulometria, di conseguenza, secondo la legge di Hall-Petch, la resistenza a snervamento aumenta seguendo l'Equazione 3.1.

Nella Tabella 3.2 sono raccolti i principali dati trovati in letteratura per quanto riguarda densità, modulo elastico, resistenza a snervamento, sforzo massimo e allungamento a rottura. Il confronto tra polveri GA e WA non può essere completo a causa della mancanza di dati presenti in letteratura. Dai dati a disposizione si evince che i campioni WA hanno un minore allungamento a rottura, a causa di una maggiore presenza di Si.

L'ottimizzazione dei parametri di processo ha l'obiettivo di massimizzare la densità, in quanto essa ha un'influenza positiva sulle proprietà meccaniche [42]. Molti studi si concentrano sulla VED e sull'influenza di questo parametro sulle proprietà meccaniche. Deev et al. [67] affermano che aumentando la potenza del laser anche la resistenza a snervamento aumenta. Se la potenza però cresce eccessivamente allora la resistenza a snervamento cala [75]. Una maggiore *scanning speed* può generare una struttura con grani più fini a causa del minor flusso di calore e di conseguenza una maggiore resistenza a snervamento, secondo la legge di Hall-Petch. Diverse fonti propongono varie metodologie di scansione per migliorare la struttura cristallina e aumentare il carico di snervamento, come gli esempi riportati in Figura 3.8.

L'anisotropia è una caratteristica tipica dei processi di manifattura additiva a causa del processo di produzione per strati. La coesione del materiale è maggiore all'interno dello stesso strato e minore tra strati differenti. Una spiegazione dell'anisotropia viene fornita da Kim et al. [30], i quali affermano che le diverse proprietà meccaniche lungo le direzioni sono riconducibili alla relazione di Hall-Petch. Infatti, i grani prodotti tramite LPBF mostrano una forma allungata nella direzione di costruzione del componente, una dimensione maggiore dei grani lungo la direzione *z* è associata ad una minore resistenza a snervamento, al contrario sul piano XY la granulometria fine permette il raggiungimento di un maggiore carico a snervamento. La differenza è quantificata tra il 10% e il 15% passando da considerare i valori ottenuti lungo l'asse *z* a quelli ottenuti lungo direzioni trasversali ad esso. Ni et al. [71] hanno mostrato come cambiano le proprietà meccaniche al variare dell'angolo tra la direzione di crescita e l'asse di applicazione dello sforzo, la resistenza a trazione è massima ad un angolo di 0° e decresce all'aumentare dell'angolo, analogo andamento è seguito dall'allungamento a rottura.

Le superfici di frattura rivelano l'influenza della VED, infatti in Figura 3.10 sono confrontate micrografie di campioni con diverso comportamento, provini prodotti con minore VED mostrano la presenza di *balling*, fenomeno assente in campioni prodotti con elevata VED. Un ulteriore parametro che influisce sulle caratteristiche della superficie di rottura è il *layer thickness*; infatti, un elevato spessore può comportare la formazione di cricche a causa del *lack of fusion*. Anche la dimensione delle polveri influisce sulla frattura, infatti polveri fini portano ad una frattura duttile, mentre polveri più grossolane portano ad una frattura più fragile.

La rugosità superficiale dei componenti prodotti è studiata a causa della sua importanza nelle applicazioni ingegneristiche. Se si considera un prodotto laminato a caldo come confronto con le tecnologie tradizionali, si nota come il processo LPBF produca componenti con una peggiore finitura superficiale. Si passa dai 2 – 4 μm della laminazione a 5 – 15 μm del LPBF. Il confronto tra i diversi tipi di polvere risulta in una superficie con minore rugosità nel caso delle polveri GA. In Tabella 3.3 sono riportate diverse rugosità superficiali ottenute trovate in letteratura. In alcuni casi è possibile ricorrere al processo di *remelting*, quest'ultimo consiste in una seconda scansione ad opera del laser che permette di ottenere una migliore rugosità superficiale dello strato sottoposto al processo. Se questo processo viene ripetuto su ogni strato si verifica un aumento della densità. La rugosità superficiale è influenzata dai parametri di processo, in particolare dalla VED. L'aumento della VED comporta una superficie meno rugosa, ma un eccessivo innalzamento dell'energia può portare ad una diminuzione della finitura superficiale [60]. Inoltre, gli intervalli ideali di VED per la rugosità superficiale e la densità non coincidono [89]. Una grande influenza è esercitata dal *layer thickness*, infatti elevati spessori dello strato comportano una scarsa finitura superficiale. L'analisi di strutture sospese evidenzia una differente finitura superficiale, infatti, si riesce ad ottenere una migliore finitura superficiale nelle superfici superiori rispetto a quelle inferiori.

Un confronto completo tra polveri GA e WA deve includere anche una discussione riguardante i costi. Per questa analisi il costo globale viene diviso in due componenti, il primo riguarda i costi della macchina, mentre il secondo considera i costi del materiale. La componente relativa ai costi della macchina è riportata in Equazione 3.2, vengono inclusi l'ammortamento del macchinario, i costi relativi al gas protettivo e all'energia consumata. La seconda componente relativa al materiale è espressa dall'Equazione 3.3, in questa considerazione rientrano le quantità di materiale utilizzato, modificato attraverso dei parametri correttivi, e il tempo necessario al completamento del componente. Inserendo i valori in Tabella 3.4 si possono ricavare i costi globali. Si ottiene quindi un costo di 28.1 euro all'ora per produrre componenti con polveri GA, e un costo di 26.8 euro all'ora per polveri WA. Questa differenza di spesa deve essere considerata insieme alle altre proprietà del componente per valutare quale sia la strada migliore da seguire.

Materiali e metodi

La parte sperimentale della tesi consiste nella produzione e successiva analisi di provini di forma cubica per valutare accuratezza dimensionale, densità e rugosità superficiale. Successivamente si selezionano i parametri di processo migliori per ottenere componenti con densità ottimale e con essi vengono prodotti provini per prove a trazione.

Le polveri di partenza utilizzate sono polveri GA di EOS e polveri WA di Pometon, la composizione chimica è riportata in Tabella 4.1. Le dimensioni delle polveri sono nell'intervallo 15 – 50 µm. Le polveri sono state trattate un ora a 180°C per rimuovere tracce di umidità.

Sono stati prodotti 16 cubi di lato 12 mm per entrambi i tipi di polvere, seguendo il DoE riportato in Tabella 4.2. I parametri non inclusi sono la potenza del laser impostata a 95 W e il *layer thickness* a 25 µm. La velocità di scansione è stata variata su quattro valori, mentre per l'*hatch spacing* sono stati selezionati cinque valori differenti. Un ulteriore parametro variato è la strategia di scansione, metà dei campioni sono stati prodotti usando la strategia riportata in Figura 4.3a mentre la seconda metà quella riportata in Figura 4.3b-c.

Una volta prodotti i campioni e rimossi dalla piattaforma si è proceduto alla misurazione dei provini per valutarne l'accuratezza dimensionale, le misurazioni sono state effettuate con un calibro e ripetute per tre volte. Per la valutazione delle densità i campioni sono stati pesati a secco per conoscere la massa e, successivamente, pesati immersi in acqua. Come espresso nelle Equazioni 4.1 – 4.3 è stato possibile calcolare la densità dei campioni utilizzando il principio di Archimede, anche in questo caso le misure sono state effettuate tre volte. Le misurazioni della rugosità superficiale sono state ottenute con un rugosimetro, le superfici analizzate sono state quella superiore e le quattro laterali. Per ogni faccia è stata rilevata tre volte la rugosità e un profilo di rugosità. Le prove di trazione sono state svolte a deformazione costante di 2 mm/min a temperatura ambiente.

Risultati e discussione

I risultati delle misurazioni dei campioni hanno fornito i dati in Tabella 5.1, dai quali si evince che, anche se in maniera molto lieve, i campioni GA hanno una migliore accuratezza dimensionale.

Le misure di densità hanno fornito risultati concordi con la letteratura, i campioni GA mostrano una densità maggiore rispetto ai campioni WA come si evince dalla Tabella 5.2. È importante notare come i campioni più densi per ogni categoria siano il GA14 e il WA09, in questo caso non si ottiene la densità massima con lo stesso set di parametri di processo per entrambi i tipi di polvere. I valori ottenuti sono concordi con le fonti in letteratura che spaziano dal 95.7% fino al 99.9%.

Table 5.2 The relative density of samples produced with gas atomized powder on the left, while the relative density of samples built using water atomized powder on the right side.

Sample	Relative Density (%)	Sample	Relative Density (%)
GA01	99.41	WA01	97.17
GA02	99.29	WA02	97.65
GA03	98.71	WA03	97.07
GA04	96.67	WA04	96.13
GA05	99.39	WA05	96.62
GA06	99.29	WA06	98.11
GA07	98.79	WA07	98.13
GA08	96.48	WA08	95.65
GA09	99.48	WA09	99.02
GA10	99.40	WA10	98.35
GA11	99.12	WA11	97.86
GA12	97.62	WA12	97.18
GA13	99.52	WA13	96.29
GA14	99.63	WA14	97.12
GA15	99.46	WA15	98.11
GA16	97.87	WA16	97.58

Oltre al tipo di polvere, anche i parametri di processo influenzano la densità. Per i campioni GA si nota come un incremento della VED, all'interno del range utilizzato in questo lavoro, produca un iniziale innalzamento della densità seguito da una zona in cui la densità rimane costante. Nel caso dei campioni WA, si nota un iniziale incremento della densità all'aumentare della VED, ma, successivamente, si verifica una diminuzione della densità per valori di VED elevati. Anche la strategia di scansione influisce sulla densità, infatti, generalmente, la strategia *Stripes* produce campioni più densi rispetto alla strategia *Chess*.

La velocità di scansione influisce sulla densità, infatti all'aumentare della velocità del fascio la densità decresce per entrambi i tipi di polvere utilizzata. I campioni GA presentano un'inziale fase in cui la densità cala leggermente seguita da un netto calo per velocità elevate, come riportato in Figura 5.3a. L'effetto dell'*hatch spacing* invece è differente per i due tipi di polvere. I campioni GA mostrano un andamento circa costante della densità all'aumentare dell'*hatch spacing* mentre per valori elevati di quest'ultimo si verifica un calo della densità. I provini WA, invece, mostrano un aumento della densità al crescere dell'*hatch spacing* fino ad arrivare ad un picco dopo il quale si ha una diminuzione della densità.

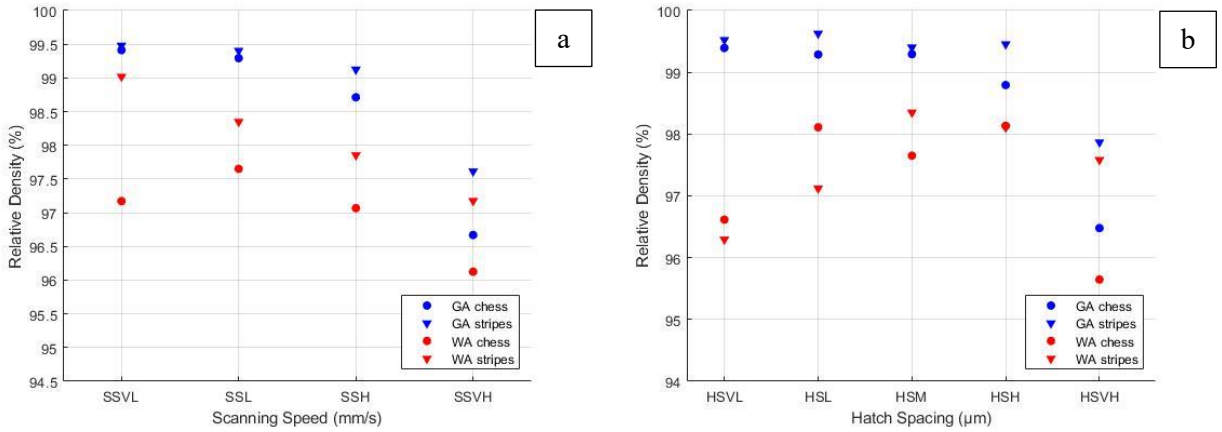

Figure 5.3 Relative density as a function of (a) scanning speed and (b) hatch spacing.

Per la produzione dei provini per le prove di trazione è stato selezionato come set di parametri di processo da utilizzare quello che massimizza la densità dei campioni GA.

La rugosità superficiale è stata analizzata e i risultati sono concordi con le fonti bibliografiche. Infatti, le superfici superiori con la minore rugosità hanno riportato valori di 7.89 µm per il campione GA06 e 10.59 µm per il WA12. Si nota che generalmente i campioni prodotti con polvere GA mostrano una migliore finitura superficiale. Anche in questo caso è necessario verificare l'andamento della rugosità in funzione della VED, per quanto riguarda i campioni WA si nota come la rugosità cresca all'aumentare della VED. Al contrario la rugosità diminuisce al crescere della VED fino ad un picco minimo per i campioni GA. Le rugosità di tutti i provini sono molto simili per bassi valori di VED, per poi differenziarsi all'aumentare di quest'ultima.

Le superfici laterali mostrano una rugosità minore rispetto alla superficie superiore. L'andamento è pressoché costante in funzione della VED, con la differenza che in questo caso i provini WA presentano una migliore finitura superficiale.

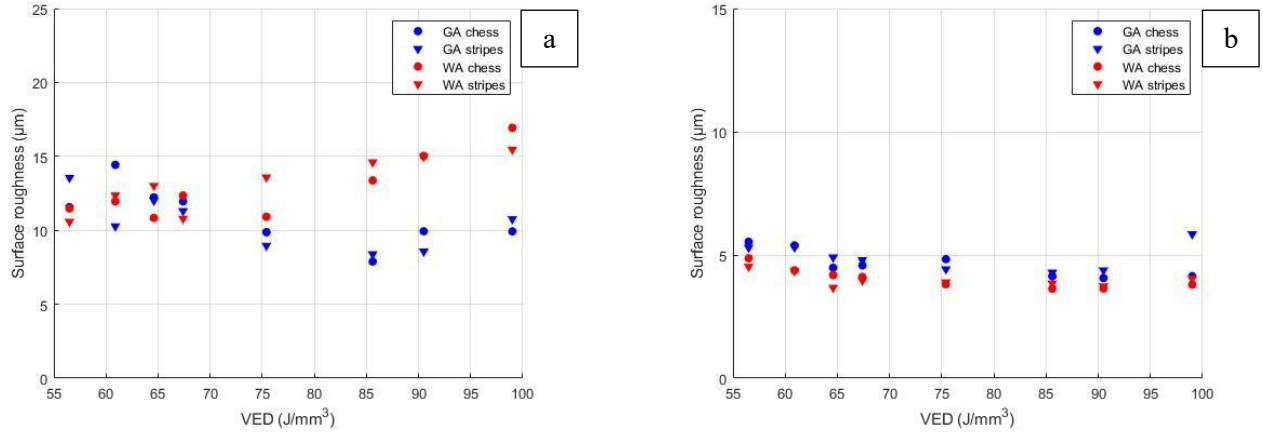

Figure 5.4 Surface roughness as a function of VED for (a) top surface and (b) lateral surface.

Analogamente alla densità, anche la rugosità superficiale è influenzata dai parametri di processo. All'aumentare della velocità di scansione si nota come la rugosità abbia comportamenti opposti per i due tipi di provino; infatti, cresce per i provini GA e diminuisce per i provini WA. L'effetto dell'*hatch spacing* è differente, all'aumentare

di quest'ultimo la rugosità dei campioni WA diminuisce mentre i campioni GA presentano una breve diminuzione della rugosità seguita da un aumento per valori maggiori di *hatch spacing*.

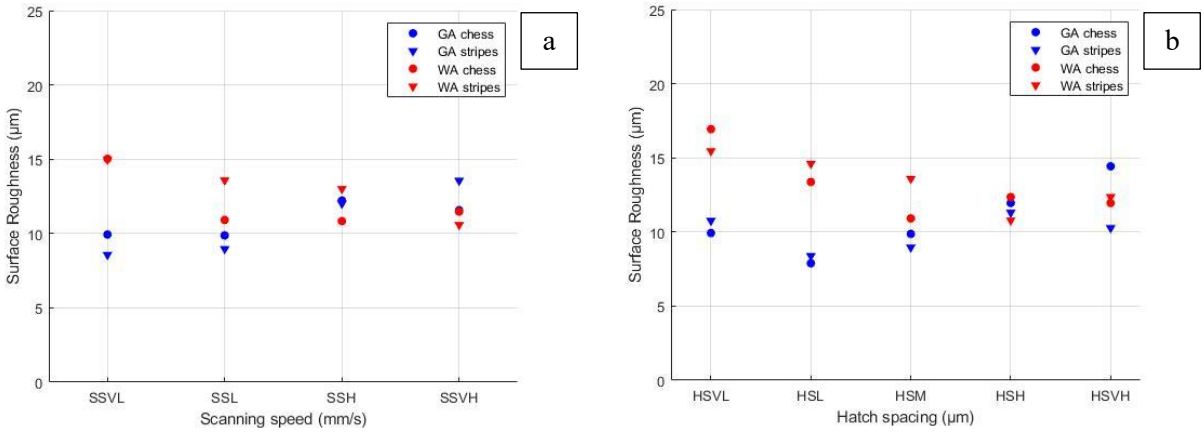

Figure 5.6 Surface roughness as a function of (a) hatch spacing and (b) scanning speed.

I provini utilizzati nelle prove di trazione sono 8, di cui 5 GA e 3 WA, inoltre essi sono stati prodotti orizzontalmente sulla piattaforma, questa orientazione garantisce migliori proprietà meccaniche lungo l'asse del provino come precedentemente affermato. Le differenze nei due tipi di provini si manifestano nella resistenza a snervamento, in cui i provini GA raggiungono i 505 – 540 MPa mentre i provini WA si attestano sui 460 – 480 MPa. Questi valori trovano conferma in letteratura [27]. Anche per quanto riguarda i valori di resistenza a trazione i risultati sono in accordo con la letteratura, inoltre anche in questo caso i provini GA mostrano migliori proprietà. I due tipi di provini mostrano comportamenti diversi nelle prove di trazione. Infatti, i provini WA mostrano un maggiore allungamento in corrispondenza dello stress massimo rispetto ai provini GA, successivamente la fase di strizione è molto breve per i provini WA e di conseguenza l'allungamento a rottura è molto maggiore per i provini GA.

Table 5.3 Mechanical test results. Yield strength (YS), ultimate tensile strength (UTS), elongation at maximum stress (ε), elongation at failure (ε_f)

Sample	YS [MPa]	UTS [MPa]	ε (%)	ε_f (%)
GA01	522.9	617.6	17.76	24.34
GA02	516.2	611.4	17.08	24.83
GA03	539.5	614.9	18.38	25.49
GA04	517.6	608.6	18.81	27.03
GA05	506.2	599.8	18.74	25.82
WA01	464.6	576.5	21.15	22.63
WA02	480.2	596	18.2	19.57
WA03	464.4	573.3	19.31	20.16

Conclusioni

Le principali evidenze sperimentali raccolte sono riportate in questa sezione.

L'accuratezza dimensionale è maggiore nei campioni prodotti con polvere GA. Anche la densità, generalmente, è maggiore per i campioni GA, la densità massima è raggiunta in corrispondenza di due diversi set di parametri di processo. L'aumento della VED produce un aumento della densità, ma nel caso di provini WA si ha una decrescita per valori eccessivamente alti.

La rugosità superficiale mostra andamenti differenti tra le facce laterali e quella superiore, le prime posseggono migliore rugosità superficiale. Considerando le superfici superiori per bassi valori di VED la rugosità è confrontabile, all'aumentare della VED invece i provini GA mostrano una diminuzione della rugosità superficiale; i provini WA hanno andamento opposto. I provini WA presentano una migliore finitura superficiale sulle superfici laterali in confronto ai provini GA. Inoltre, come visibile dai risultati, è impossibile ottimizzare contemporaneamente la densità e la rugosità superficiale.

Per quanto riguarda le proprietà meccaniche, i provini GA mostrano migliori resistenze a snervamento e a rottura. La principale differenza è nel comportamento dei provini dopo il raggiungimento del massimo livello di stress. Infatti, i provini GA continuano la loro deformazione mentre i provini WA arrivano prima a frattura.

2. Introduction

This thesis work concerns the study of the effects of different types of powder used as a feedstock material in an additive manufacturing process, particularly the laser powder bed fusion (LPBF) process. The powder is the raw material used in this kind of process. The powder features, such as shape and chemical composition, influence the properties of the final product; in this specific case, the features analyzed are the surface roughness and the mechanical properties.

This work aims to cover a lack in the literature. Due to the specific features of the powders, most of the information is about one type, the gas atomized powders. The other type, water atomized powders, is not deeply investigated due to the irregular shape and the chemical composition. The first part of this work is a review of the information in the literature and a comparison of the results achieved by different authors. The second part is an experimental analysis in which samples are produced and analyzed comparing the two types of feedstock material.

This thesis is composed of 5 parts. After a brief introduction to the production technology and of the material analyzed, the second part investigates the general state of the art, producing a comparison of two types of feedstock material. The third section is about the material and methods used in the experimental analysis. The fourth is a report with a relative discussion of the results of the analysis. Finally, the last part includes the general conclusions from the results and state of the art.

In recent years, additive manufacturing (AM) reached a significative use in many industries, such as aerospace [1,2], automotive [3,4], and biomedical sectors [5,6]. The driving force of its development is the freedom about shape; indeed, AM allows to build components with complex geometries, which are difficult to obtain by means of traditional techniques [7]. Furthermore, the specific designs that can be realized via AM lead to a weight reduction in the components due to the possibility of putting material only where necessary[8]. The concept of all AM processes is layer by layer production in which, at first, the CAD model of a final component is designed and sliced in many layers; their thickness depends on the features of the specific AM process used for the production. Thereafter, during the production phase, in each layer selective regions are melted through a suitable heat source such as laser, electron beam, electric arc [9]. The heat source is driven on a specific scanning path to melt the section prescribed by the sliced CAD model.

In general, metal AM processes can be divided into two macro groups, Powder Bed Fusion (PBF) [10,11], or powder (or wire) feed system, also called Directed Energy Deposition (DED), [12,13]. The PBF one can also be subdivided into laser powder bed fusion (LPBF) and electron beam melting (EBM) according to the heat source, one or more laser or an electron beam, respectively [14]. In both of them, the powder is spread on a building platform by a raking system, and the heat source melts only the desired section according to the CAD file [15]. However, in LPBF, the laser beam does not affect the surrounding powder, whereas each powder layer is partly sintered before the melting phase in the EBM process. Instead, in the DED process based on powder or wire, the feedstock material is delivered in the localized molten pool through a deposition head which also provides the heat source. LPBF can achieve, as well as AM technologies, high geometrical complexity, challenging for conventional ones. The complex geometry allows the creation of components with optimized shapes to support loads with the minimum quantity of material. This weight reduction has a primary appeal in the automotive and aerospace industries. The LPBF, the EBM, and the DED are the three most common metal AM processes; every process has its features. For example, the thickness of each layer is different in every process; LPBF has a layer thickness of around 20 and 50 µm, while EBM (data according to Arcam A2X datasheet) ranges from 50 to 250 µm, the DED has the possibility of reaching up to 600 µm [9]. Another factor correlated to layer thickness is the build rate; indeed, according to manufacturers, LPBF can reach up to 200

cm^3/h, while EBM has lower productivity due to the pre-heating of powders and the post-processing needed. On the other hand, the production rate of LPBF is lower than DED's one. As compared to other metal AM processes, LPBF has the highest dimensional accuracy and lowest surface roughness. Moreover, the atmosphere is a feature of each process; due to the presence of the electron beam in EBM, the atmosphere must be at low pressure, 10^{-3} Pa. Indeed, in the case of DED, the nozzle also provides a shielding gas to avoid oxidation of the melt pool. The feedstock material must be selected in the proper way for each process. For example, in LPBF, the powder dimension usually is under 50 μm, while in DED, the powder is coarser and can reach up to 150 μm of dimension; in EBM, the particle size ranges between 45 and 105 μm. The supports need for overhang structures is an additional drawback. Indeed, support elimination is a further and problematic step, not required in EBM. On the other hand, some technologies such as DED cannot build overhang structures due to the impossibility of building supports.

Various denominations are given to the LPBF process due to commercial reasons. Table 2.1 summarizes the commercial names that have been proposed so far.

Table 2.1 Different commercial names for the LPBF process.

Acronym	Technology	Reference
SLM	Selective Laser Melting	[16,17]
LC	Laser Cusing	[18,19]
DMLS	Direct Metal Laser Sintering	[20,21]

In general, the LPBF process, schematically shown in Figure 2.1, is divided into three main steps repeated during the building process. The cycle begins with the spreading of powder on the building platform [22]. In fact, the feedstock material dispenser provides powder then a recoater blade spreads them over the building platform. The quantity of powder and the altitude of the blade are set finely to obtain the desired layer thickness. Once the powder bed is created, the laser proceeds to selectively melt it, overlapping two consecutive layers in order to create a solid bonded structure. The laser source is stationary, so the beam is focused and moved by f-θ lenses. At the end of the scanning step, the building platform is lowered down equal to a layer thickness; at this point, the cycle restarts and continues until the building is completed.

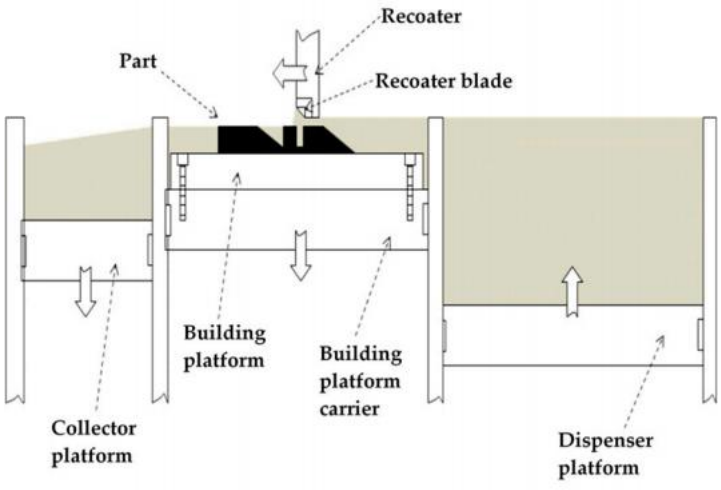

Figure 2.1 Schematic of a LPBF process [23].

In the LPBF process, many variables can affect the properties of the final component. Complete control over all those parameters allows achieving full densification as well as desired mechanical properties, surface quality, acceptable tolerances, and sustainable production rate. For instance, Gusarov et al. [24] divided process parameters into three main categories. The first one includes power source features such as power, wavelength, focus diameter, but it also includes scanning strategy and speed. Additionally, the scanning strategy implicitly

includes the hatch space, the distance between the center of two subsequent melt pools. The second group is of parameters related to an atmospheric condition such as its composition, heat conduction properties, environment, platform temperature, and oxygen content in the building chamber. The third and final group of parameters is associated with material, such as its composition and thermal properties, which can affect heat distribution, the size and shape of starting powder, and the layer thickness of the powder bed. Detailed discussion about optimization of process parameters is provided further in this work, especially laser power, scanning speed, hatch spacing, and layer thickness.

Stainless steels succeeded to pique interest mainly due to their high performance and their high mechanical properties. Indeed, various applications require the ability to withstand an aggressive environment [25]. For example, in the biomedical field, the component is in continuous contact with body fluids; in this sector, the high corrosion resistance of austenitic stainless steels is their strength. Another edge of austenitic stainless steel is the high erosion resistance; the components can resist the effect of erosive particles [26]. In addition, mechanical properties make this type of material suitable for many engineering applications. The set of these features makes these materials interesting, and thus the properties are widely investigated. AISI 316L is one of the most studied austenitic stainless steel. As a result, it is possible to design various components to be produced in this material, combining the excellent features of the 316L and the general advantages of additive manufacturing, such as the geometrical complexity achievable,

As shown in Figure 2.2, the interest in 316L as feedstock material in the SLM process has risen over the years and has a similar number of published papers compared with all other stainless steel. Figure 2.3 subdivides all the found papers into topics. The copious part of all published papers concerns mechanical properties.

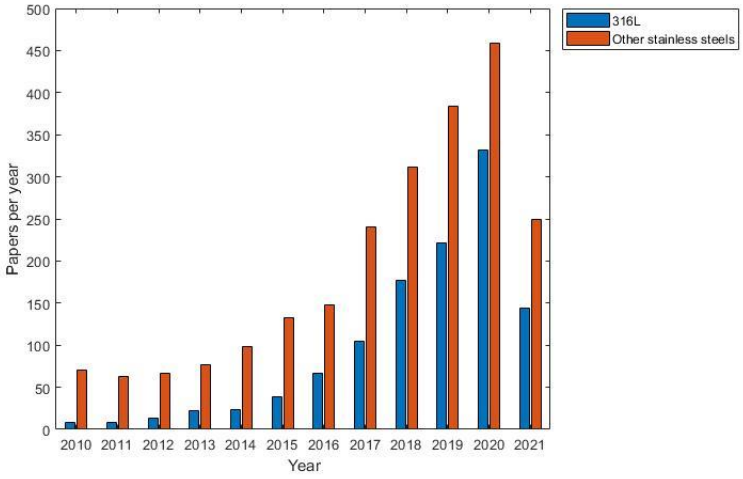

Figure 2.1 The number of published papers per year from www.sciencedirect.com. Results were produced by searching "stainless steel SLM" and "316L SLM".

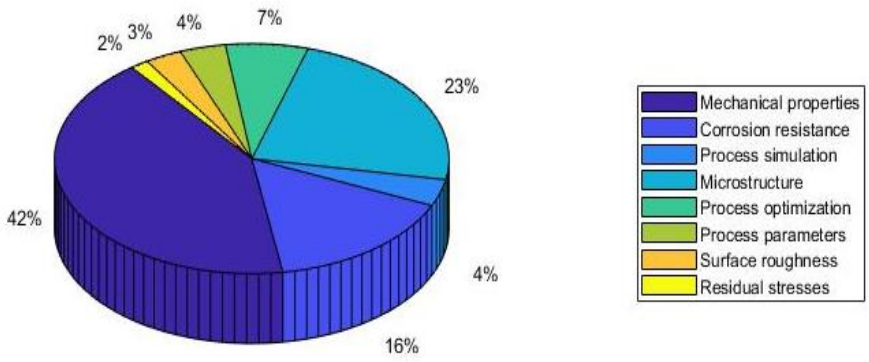

Figure 2.2. Percentage of published papers on different themes. Results of "316L SLM" search on www.sciencedirect.com.

This job aims to collect the information available in the literature about the AISI 316L manufactured via LPBF. The purpose is not to group information from different sources but rather to compare the various results and provide further explanation. Due to the features of two types of powder, which will be analyzed later, gas atomized powder has a broader use to water atomized powder. For this reason, the majority of data and information are focused on gas-atomized powder.

3. State of art

3.1 Feedstock material

LPBF feedstock material is provided in the form of powder with an average particle size of usually under 65 μm [27–30]. The powder used to produce the powder bed has a crucial influence on all the following properties. Indeed, the quality of the final product can be different and strongly depends on the features of the powder. More precisely, the powder bed factors are how easily the powder spreads and how dense the bed can be obtained. The flowability is the first main feature; according to Strondl et al. [31], high flowability is mandatory to obtain a homogeneous powder bed. The powder can be easily spread if the aspect ratio is close to one [32,33]. Thus, spherical particles show better flowability than irregular ones. Kiani et al. [34] state that powder with low surface roughness shows better flowability than rougher powder. Due to the higher specific surface, the finer particles can be affected by Van der Waals forces, which can produce agglomeration; the effect on the flowability is harmful, according to Hoeges et al. [35]. The second main feature is the packing ability of powders. The spherical powder can pack with a limited quantity of holes between particles. Oppositely, the irregularly shaped powder can pack in a less dense powder bed [34]. Therefore, agglomerates can be considered as irregularly shaped powder.

The metallic powder is obtained through an atomizing process, and many methods can be used. In the following paragraph, the powders obtained through water atomizing (WA), gas atomizing (GA), and plasma atomizing (PA) are compared. The first feature of the atomized powder is the shape. In the GA process, the inert gas flow (usually nitrogen or argon) creates a high thermal gradient and, consequently, rapid cooling, generating a spherical particle. In the WA process, the thermal gradient is lower, and the shape is irregular. Oppositely, in the PA, the slow and controlled process allows the production of very spherical powder. The low oxygen presence is a strength of the PA process due to the excellent purity achievable; the GA powder has an oxygen content in the range of 100 – 500 ppm, while WA introduces more than 500 ppm of oxygen in the powder [36]. Oppositely to oxygen presence, the high cost is the major drawback of PA because of the low production rate. Water atomizing is cheaper than GA [37].

Considering all the features relative to the different atomizing processes and the general requirements for LPBF feedstock material highlighted in the previous paragraphs, it is possible to explain the powder selection process. The GA and PA powder can comply with the request the excellent flowability due to its spherical shape, while the WA produces irregular powder morphology. The different morphological aspect of 316L powder, obtained from GA and WA, is shown Figure 3.1 (a,b). Due to the high cost of PA powder, GA and WA powder are the most used. In particular, the GA powder is the best compromise [32,33,35,36]. According to Riabov et al. [36], the GA process introduces a higher nitrogen content in the powder composition (0.14 and 0.04 wt.% in gas and water atomized 316L powder, respectively), similar to what happens with oxygen in WA.

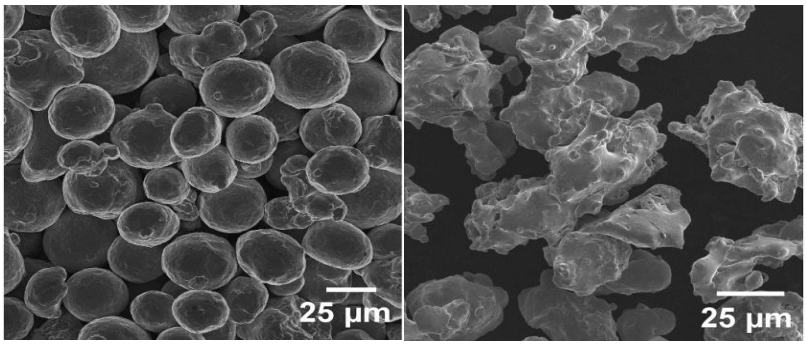

Figure 3.1 AISI 316L (a) gas atomized powder, and (b) water atomized powder [36].

Oxygen introduced in steel microstructure can produce embrittlement and consequentially a drop of mechanical properties [38]. On the other hand, in some cases, this impurity can be turned into a positive presence, as explained by Riabov et al. [36], that reached an increase of component mechanical properties due to oxide dispersion strengthening obtained after thermal treatment. Moreover, the manganese content is lower in water atomized powder because, according to Hoeges et al. [35], the oxygen introduced can quickly produce oxides during the atomizing process. In the LPBF process, the feedstock material can be recycled to a large extend because during the process, the powder bed is melted selectively, and thus it is possible to reuse the rest of the unmelted powder, according to Yusuf et al. [39]. However, the recycled powders show some slight differences compared to those of virgin ones. Indeed, the recycled powders have a coarser size range; this enlargement is due to the melting of smaller particles during previous scanning steps. Nevertheless, dimensions are not the only change in recycled powders with higher oxygen content, as reported by Cordova et al. [40] and Tang et al. [41]. This oxygen surplus leads to significant composition modification and mechanical properties consequently.

3.2 Process parameters optimization

One of the first experiments dealing with the LPBF process is the optimization of process parameters to find the appropriate process window for each material. The main goal of this method is to achieve the maximum density for the component in the as-built state. The optimization carries out by experimental trials following the design of experiment (DoE) approach, whereas the computerized prediction suffers from complex numerical analysis due to the substantial number of involved parameters. Nevertheless, Tian et al. [42] proved that through the optimization of process parameters, it would be possible to reach the maximum density close to its theoretical value and consequently obtain the maximum mechanical properties in the as-built state. Figure 3.2 shows the relationship between residual porosity and volumetric energy density (VED) in the as-built 316L samples produced via the LPBF process.

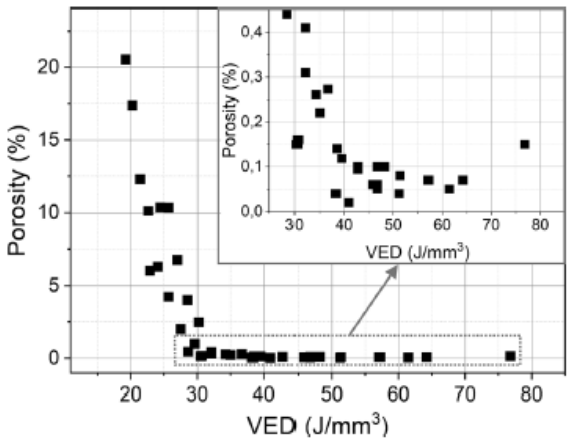

Figure 3.2 Porosity content as a function of VED in 316L samples made by the LPBF process [43].

As shown in Figure 3.2, the porosity percentage of the samples significantly changed in two regions with higher VED and lower VED. The latter is not optimal because VED involves the formation of pores due to lack of fusion, according to Greco et al. [17]. In fact, in this region, the input energy is insufficient to obtain a homogeneous melting on the scanning track; so some parts of the powder bed do not melt or are only partially melted. On the other hand, high energy allows raising the melting temperature and, consequently, induces overheating and boiling of material. These gas-induced pores, which result from gas entrapment inside the melt pool, are also known as keyhole defects [44]. Moreover, King et al. reported that the laser could penetrate more in-depth once gas leaves the melt pool [44]. Thus, in general, VED is a critical factor that shows the effect of

the combination of process parameters on the final defect content of the component. However, it should be underlined that VED includes some process parameters such as laser power (*P*), layer thickness *(Lt*), hatch spacing (*Hs*), and scanning speed (*υ*), as shown in Equation (3.1).

$$VED = \frac{P}{L_t \times H_s \times \vartheta} \tag{3.1}$$

In principle, over the last years, optimization of process parameters through the DoE approach and VED has been considered as one of the main methods to find the optimum process parameters [45]. In this approach, a different combination of process parameters that give different levels of VED is considered. After the sample production, the residual defect content such as porosity or crack highlights the best VED and, consequently, process parameters. In this approach, the effect of each parameter is evaluated at the other constant process parameters. The first parameter investigated is laser power (*P*). This parameter can be limited in some LPBF machines with low laser power. In general, in the market, there are several machines with different laser powers ranges from 100 W to 1000 W [46]. The variation of this process parameter on the consolidation behavior of the AISI 316L has been studied by Greco et al. [17] and Laakso [47] et al., both works confirm that at a constant VED, the density of as-built AISI 316L samples increases by raising the laser power. The experimental output of Deng et al. [48] provided a similar trend, but at high laser power, they found keyhole defects in the as-built samples. The second examined parameter is the hatch spacing; however, in this case, switching the laser spot size involves different effects. In Greco et al. [17] work, different hatch spacing and scanning speed values are studied, keeping the VED constant. Their results exhibited an increase in density by raising hatch spacing. However, it should be highlighted that the range of hatch spacing should be tuned carefully to avoid the formation of process-induced porosity (lack of fusion) and the gas-induced one. Dong et al. [49] found that the maximum consolidation and relative density can be achieved using an optimal range of hatch spacing from 75 to 100 μm, while the laser spot size is 50 μm. Below this range, the process would not be productive, and also there would be a risk of overheating and keyhole formation due to the remelting of a large fraction of already solidified material. Instead, above the optimal range, some parts remain unmelted, and consequently, some pores that are mainly the lack of fusion remain in the as-built specimens. A similar trend is reported by Sun et al. [50]. The last process parameter analyzed is the layer thickness; in this case, Greco et al. [17] reported that higher layer thicknesses at a constant VED led to lower material densification and higher defect content in the samples. This trend was explained by heterogeneous heat distribution on the powder layer. In fact, the deeper part of the powder bed received less heat due to difficult penetration. However, Shi et al. [51] stated that it is possible to achieve density over 99.5% of theoretical one, with 250 μm layer thickness, through a correct optimization of process parameters.

3.3 Microstructure

The microscopical features can affect in a significant way the final component properties; for this reason, the microstructure is widely investigated. In particular, LPBF, as other AM processes, can produce a slight difference in microstructure compared with conventional manufacturing. For example, a conventionally cast 316L, after annealing treatment (one hour at 1100 °C) and water quench, shows a microstructure with 97% of γ-austenite and 3% of martensite. Furthermore, the reported average grain size is 42 μm [52]. Rottger et al. [53] confirm the latter information; the cast sample shows equiaxed grains whit an average size of 39 μm, while LPBF produces grains with an average dimension of 25 μm.

One of the reasons behind these differences is the cooling rates involved. Indeed, the heat provided by the laser can melt the powder; subsequently, the melt solidifies rapidly. The outcome of this fast cooling is a particular structure in LPBF called melt pool, which is highlighted in yellow in Figure 3.3. An optical microscope can

highlight the melt pool easily; the melt pool depth is higher than layer thickness due to a partial remelting of the underlying layer, which results in a stronger bond in the structure. Casati et al. [54] affirm that a melt pool depth of 90 μm is visible, setting a layer thickness of 50 μm. Moreover, also subsequent melt pools overlap for a portion can be noticed. The microstructure of the melt pool shows some typical features as the grain's expansion over the melt pool boundaries and directionally growth. The former feature results from epitaxial growth; when the molten metal begins the solidification process, the atoms arrange themselves with the same structure of solid substrate underlying. The growth direction is the direction of maximum heat flow [55].

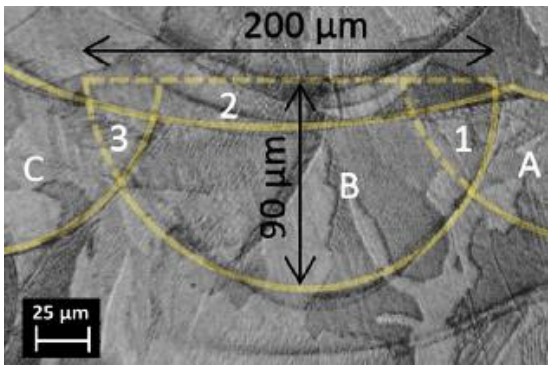

Figure 3.3 Melt pool image with dimensions. 1 and 3 are overlapping zones with melt pools A and C, respectively. 2 is an overlapping zone with the upper melt pool [54].

Further microstructural analysis can investigate the different present phases by the XRD machine. Generally, the analysis results show a phase composition of 100% austenite (γ) [43], [39,56–58]. However, Sun et al. [50] declared the presence of austenite (γ) and ferrite (δ) in microstructure, while Tucho et al. [59] found a non-austenitic phase, without clarifying whether it consists of ferrite (δ) or martensite. As reported in [44] and [49], the XRD spectra of the final component show some differences with the spectra of starting powder, as clearly seen in Figure 3.4. There is a broadening of peaks in the built component compared to virgin powder, a sign of a slightly different crystalline structure. The widest peak is related to residual stresses in the component because of thermal stresses. A common microstructural defect is balling, which can be detected, as in Figure 3.5, through the presence of unmelt or partially molten spheres with a maximum of 50 μm of diameter. Furthermore, the balling reduces mechanical properties and surface roughness. This kind of defect results from unsuitable process parameters, as explained by Cherry et al. [60]. An excess of energy affects wettability and consequently the solidified structure. Another cause of the balling phenomena is the lack of fusion due to the lower energy involved. Tucho et al. [59] found the presence of inclusions with a size range from few nanometers to few micrometers. They also investigated their composition and found two inclusion types shown in Figure 3.6: dark and bright spots. Chemical composition was detected using STEM/EDAX technique, discovering that bright

inclusions are losing Fe and Cr for the rest due to Fe, Cr, and Mn silicates formation. Dark inclusions are rich in Fe and Cr.

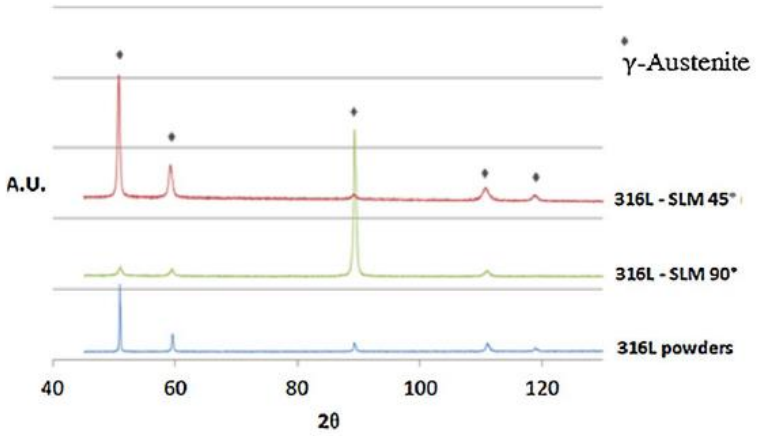

Figure 3.4 XRD spectra of powders and built components, in which is visible the broadening of peaks. 45° and 90° indicates the orientation in the building chamber [58].

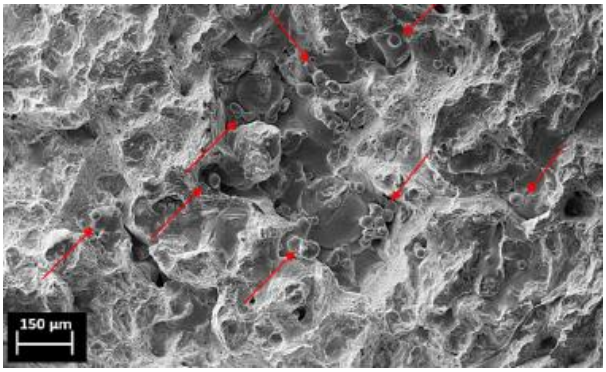

Figure 3.5 Fracture surface in which are visible spheres as a balling result [54].

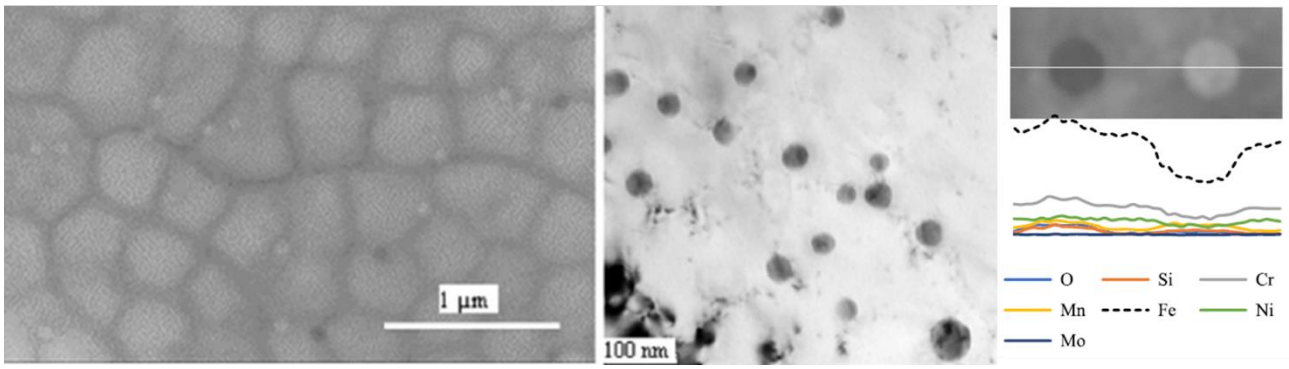

Figure 3.6 On the left and in the center images of inclusions. On the right, STEM/EDAX result of chemical composition analysis [59].

3.4 Mechanical properties

One of the fundamental aspects of the AM parts is their final mechanical performance. Therefore, much research has been carried out on this matter [10,53,61,62]. Table 3.1 simplify to compare the mechanical properties of 316L using conventional technologies, in this case, hot-rolled [63] and casting [64]. The LPBF yield strength stands out from the traditional's one; this gap does not characterize the ultimate tensile strength, which is slightly

higher in as-built samples. However, the LPBF specimens suffer from their lower elongation range compared to those of traditionally manufactured techniques

Table 3.1 YS, UTS, and ε of LPBF, as-cast and hot-rolled 316L [63,64].

Type	YS (MPa)	UTS (MPa)	ε_f (%)
LPBF	450-600	600-700	40-60
Cast	310	620	45
Hot-rolled	360	625	69

The higher mechanical strength of AISI 316L samples produced via LPBF is an edge that can favor the development of this manufacturing technique since it is possible to achieve better mechanical compared to those traditionally manufactured while keeping their excellent corrosion resistance. The increase of mechanical properties results from the high cooling rate in LPBF, generally around 10^6 K/s, while in conventional casting methods cooling rates can reach up 10^3 K/s, as reported by Wang et al. [33]. Different cooling rates lead to a different solidification process that has a significant impact on the grain size. As explained in the Hall-Petch relationship [46], microstructure influences the mechanical properties, where the grain size (d) strongly influences yield strength. Therefore, the smaller grain size explains the difference between the data reported in Table 3.1 and Table 3.2. Precisely, the Hall-Petch equation, reported as Equation 3.1, succeeds in estimate the yield stress knowing the YS_0, which is frictional stress resisting the motion of gliding dislocations in the absence of grain boundaries and, k is a constant depending on the material

$$YS = YS_0 + \frac{k}{\sqrt{d}} \tag{3.1}$$

Table 3.2 summarizes data collected in the literature about mechanical properties achieved by different researchers; the comparison between diverse feedstock materials cannot be complete due to the insufficient data about analysis on samples produced with water-atomized powders available in the literature

Table 3.2 Young modulus (E), yield strength (YS), ultimate tensile strength (UTS), and elongation at break (ε_f) are reported in the table.

Density (%)	Type of powder	E (GPa)	YS (MPa)	UTS (MPa)	ε_f (%)	Ref.
99.77	Water atomized	150	475	611	31	[35]
-	Water atomized	-	504	644	27	[36]
99.40	Gas atomized	194	-	594	-	[65]
99.80	Gas atomized	-	590	705	44	[66]
-	Gas atomized	-	554	684	36	[54]
-	Gas atomized	-	575	696	35	[67]
-	Gas atomized	-	496	563	30	[68]
98.50	Gas atomized	166	421	528	23	[53]
99.84	Gas atomized	147	483	624	34	[35]
98.04	Gas atomized	195	385	524	22	[32]
98.10	Gas atomized	-	536	668	25	[69]
99.00	Gas atomized	-	525	625	40	[29]
99.00	Gas atomized	202	-	-	-	[70]
99.96	Gas atomized	204	466	614	30	[61]
98.10	Gas atomized	-	-	620	-	[71]
-	Gas atomized	-	535	697	50	[29]
99.60	Gas atomized	-	445	585	21	[72]
99.00	Gas atomized	-	525	622	47	[73]
-	Gas atomized	-	554	666	46	[74]
-	Gas atomized	-	527	611	29	[75]

-	Gas atomized	-	601	727	-	[36]
99.00	Gas atomized	182	503	644	51	[10]
99.50	Gas atomized	-	380	569	23	[51]
97.84	Gas atomized	-	530	646	21	[27]
-	Gas atomized	-	464	593	35	[76]
-	Gas atomized	-	637	751	41	[77]
99.60	Gas atomized	200	385	650	65	[62]
-	Gas atomized	-	550	650	-	[78]
99.00	Gas atomized	205	525	775	50	[30]
-	Gas atomized	-	450	500	44	[3]
-	Gas atomized	-	565	708	31	[79]
-	Gas atomized	-	460	640	70	[80]
-	Gas atomized	-	575	615	30	[81]
99.60	Gas atomized	-	599	760	54	[16]
99.70	Gas atomized	-	440	-	54	[82]
99.90	Gas atomized	-	-	663	38	[83]
99.45	Gas atomized	-	462	584	42	[84]

Young modulus reported by Hoeges et al. [35], for sample produced with water atomized powder, is one of the lowest elastic moduli reported for 316L alloy, while Riabov et al. [36] did not provide any measurement of Young modulus. In addition, Figure 3.7 highlighted that water atomized samples have a low elongation at failure compared to those produced using gas atomized powder. According to Hoeges et al. [35], this effect can be ascribed to a higher presence of Si than samples produced with gas atomized powders and traditionally manufactured 316L.

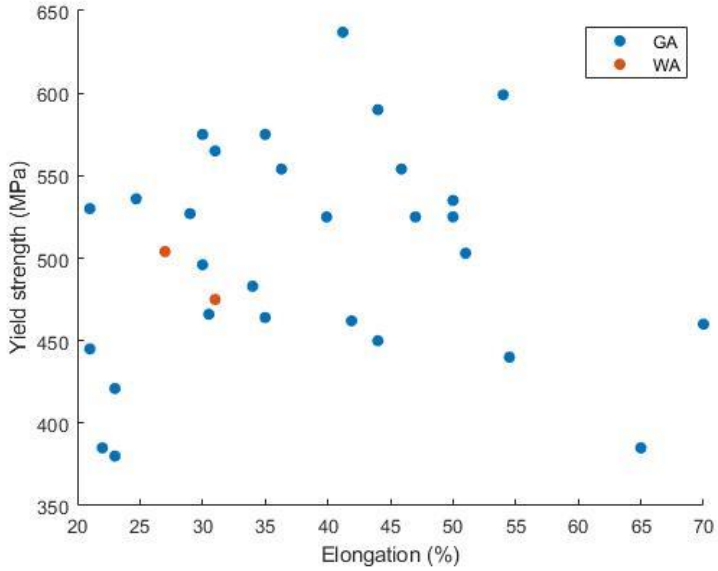

Figure 3.7 Plot of yield strength as a function of elongation of data collected in Table 3.2.

As discussed previously, the process parameters optimization succeeds in maximizing density, which remarkably influences the mechanical properties. Indeed, Tian et al. [42] reported a direct correlation between density and mechanical properties of the as-built specimens. A porosity introduces weakness into the materials and consequently jeopardizes resistance to an external load. Additionally, higher density implies uniform distribution of stresses and avoids stress concentration.

Many studies focused their attention on VED as this parameter expresses the energy provided to the powder bed and generally strongly influences the density. Deev et al. [67] reported that increasing laser power, and

consequently VED, has a positive effect on yield strength which raises. Kluczynski et al. [74] provide approximately the same results as previous work, but they specify how the yield strength drops when the laser power, and consequently VED, reach high values. Larimian et al. [84] studied the effect of scanning speed on the yield strength, finding that faster scanning, which implies lower VED, can generate a refined microstructure due to lower heat flux and, according to the Hall-Petch relationship, a higher yield strength. In the latter work, the author also claims that cross-hatches with a single scan of the laser beam, in Figure 3.8b, is the scanning strategy that provides better mechanical properties due to reduced and uniform heat flux that avoids overheating and grain enlargement. Suryawanshi et al. [69] found that the so-called chessboard strategy maximizes yield strength. The latter strategy divides the section into sectors that will be single scanned with different orientations, as reported in Figure 3.8a. Song et al. [78] adopted a rotation of scanning direction in successive layers (Figure 3.8c), allowing to interrupt the elongated columnar grains and achieve refining grain, which enhances mechanical properties. Chniouel et al. [73] studied the effect of substrate temperature on mechanical properties, becoming aware of a grain enlargement for higher temperatures and a decrease of yield strength, and an increase of elongation at break.

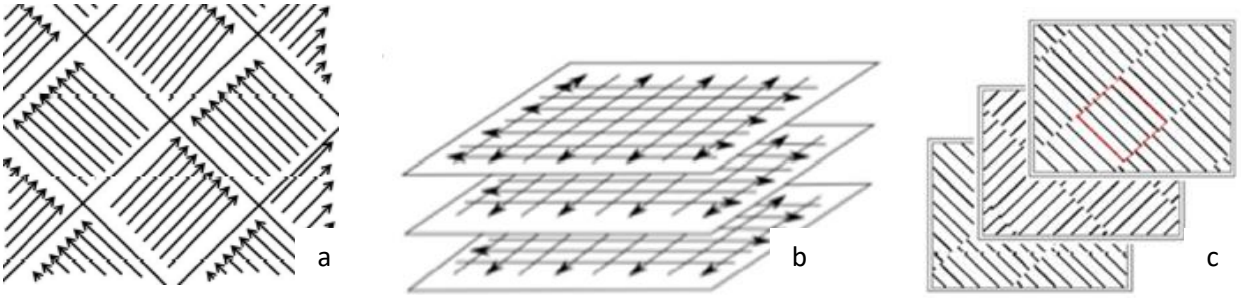

Figure 3.8 Scanning strategy adopted to improve mechanical properties, (a) chessboard, (b) cross-hatches, (c) stripes.

Many works report anisotropy of built components, which is an acclaimed feature related to the layer-by-layer production, so tensile properties are consequently lower along the building direction when compared to ones in the transverse direction. Kim et al. [30] tried to explain the anisotropy through the Hall-Petch equation. They noticed that SLM produces a microstructure with elongated grains because of the heat flux along z-direction (build-up direction); according to the Hall-Petch equation, coarser grains imply lower yield strength in the build-up axis, while in the XY plane, the grains are smaller. Thus, the yield strength is enhanced. Liverani et al. [58] provide further information. They found a decrease of 10-15% for yield strength when comparing samples built vertically with horizontal ones, a. Analyzing elongation shows a drop of 50% when passing from 45° of tilt angle to 90° (vertical built sample). Therefore, Ni et al. [71] investigated the mechanical properties of a component arranged in 5 different tilt angles in building chamber (0°, 30°, 45°, 60°, and 90°). The results are summarized in Figure 3.9a. They claim that the different properties result from different densities. Horizontally building allows for the denser sample while increasing tilt angle porosity raises. The different densities can explain the trend in Figure 3.9b except for the 30° specimen. Lavery et al. [32] confirm previous works' trend for Young modulus instead of yield strength. Liverani et al. [58] provide details about the increasing laser power effect on elongation at breaking. They explain that the latter increase is the result of the higher density reached with the upper VED. In addition to the same work, they proved that by reducing hatch spacing, the elongation increase.

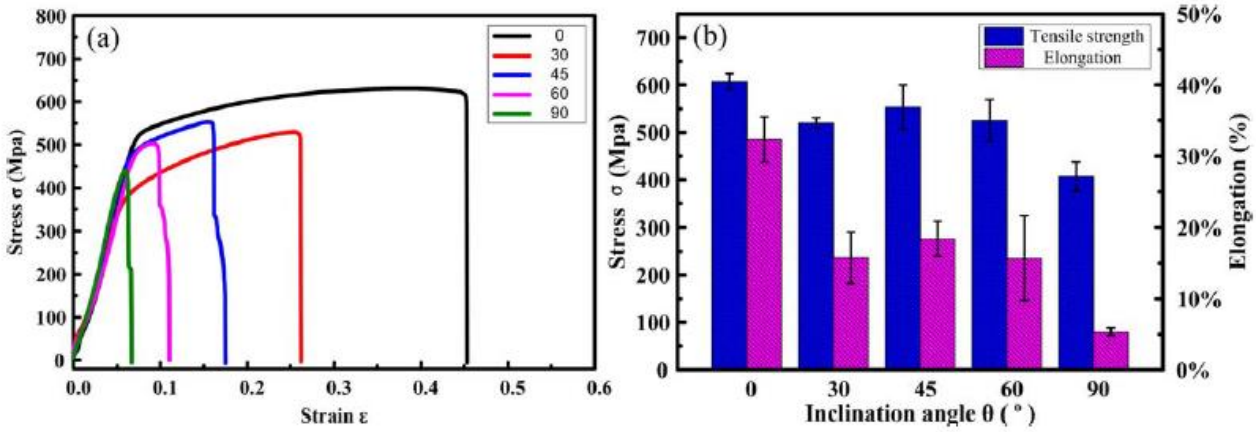

Figure 3.9 Typical stress-strain curves for tensile samples (a). Tensile properties (b) [71].

The highest result of yield strength was achieved by Kong et al. [77] in tensile tests. They reached a peak of 637 MPa due to the high dislocation concentration. Oppositely, Shi et al. achieved the minimum yield strength value of 380 MPa [51] by producing components with a high layer thickness of 250 µm, which leads to a not solidly bonded structure. However, it is noteworthy that even the lowest yield strength reported is higher than those achievable with traditional manufacturing technologies. Moreover, the optimization by the VED method affects the ultimate tensile strength achievable. The highest one is mentioned in Kim et al. [30], where the value reaches the goal of 775 MPa. The lowest UTS found in literature is 500 MPa [3] using a VED of around 5.6 $kJmm^{-3}$.

3.4.1 Fracture surface

The observation of the surface after the fracture in tensile tests can complete the analysis of mechanical properties. Therefore, this study allows checking the presence of defects and obtaining information about the kind of fracture. In the work of Leicht et al. [55] is reported the Figure 3.10 in which can be clearly visible the effect of different values of VED, 58.0 Jmm^{-3} in images a) and c) while in images b) and d) the VED is 203 Jmm^{-3}. This fractography shows the homogeneous structure in the sample with higher VED, while the balling effect affects the lower VED sample; Figures 3.10c and 3.10d display the higher magnification of highlighted zones in Figure 3.10a and 3.10b, respectively.

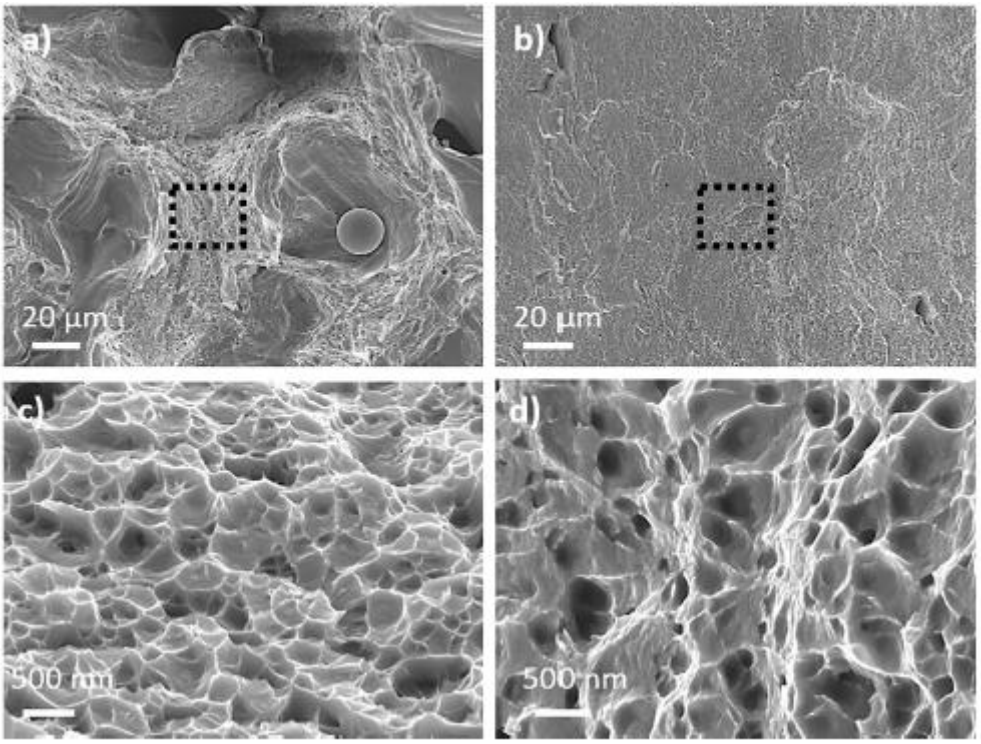

Figure 3.10 SEM micrographs of the fracture surface of specimens produced with 58.0 Jmm^{-3} (a and c) and 203 Jmm^{-3} (b and d).

Instead, figure 3.11 is an example of how to analyze fracture surfaces when using different layer thicknesses. The two shown samples are characterized by a layer thickness of 20 µm and 80 µm, whereas all other process parameters are constant. High layer thickness can produce defects or lack of fusion, negatively impacting the mechanical properties, as reported in [43].

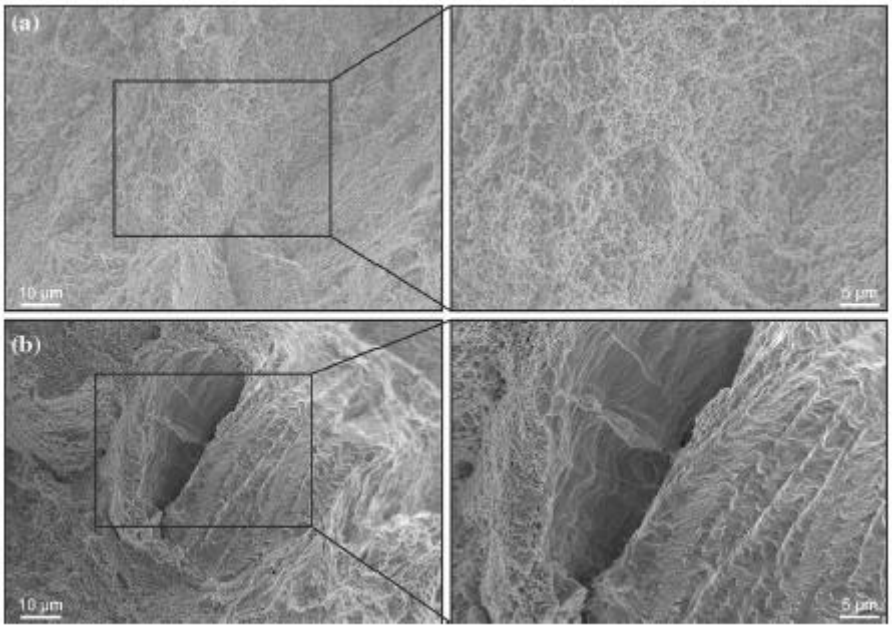

Figure 3.11 SEM micrographs of the fracture surface of two samples produced with different layer thicknesses, 20 µm in (a) and 80 µm in (b).

Another parameter that can influence the fracture surface is the size of powder feedstock. Regarding that, Chen et al. [45] show by Figure 3.12 three sizes of powder: the finer powder on the left column (16 µm), the coarser

powder on the central one (48 µm), and the raw powder (4-48 µm) on the right column. The lower magnification makes it possible to see irregular voids (marked with yellow arrow) and lack of fusion defects (marked with white arrow). From observation of the lower row, it is possible to evaluate the type of fracture. Fine powder has a more ductile fracture than raw powder, while coarse powder is more fragile. Differences in fracture surfaces are highlighted in Ni et al. [71]; in this work, different tilt angles are used during building, resulting in different fractography outcomes. As shown in Figure 3.13e, referred to as 90° of tilting angle, which means vertically built, the surface fracture shows a brittle behavior while other samples show a ductile fracture.

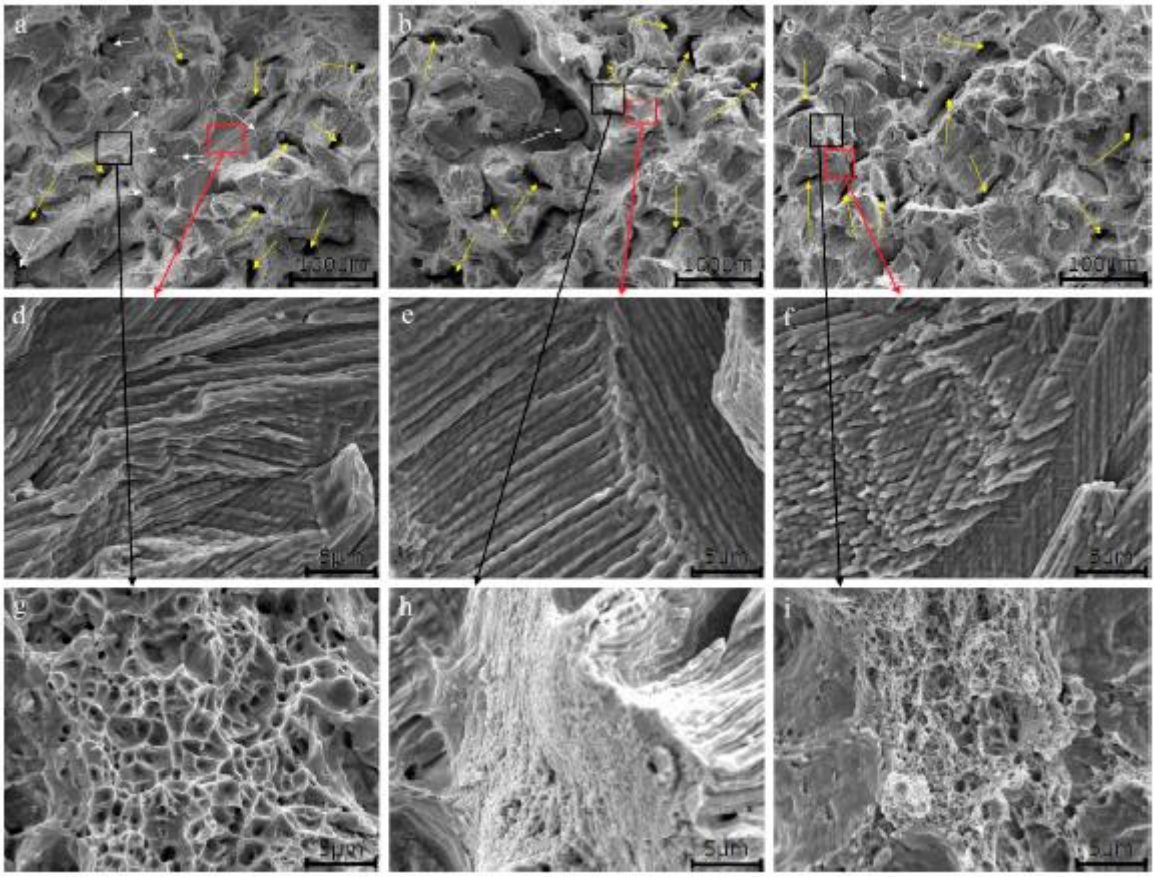

Figure 3.12 SEM micrographs of samples produced with different feedstock sizes. Fine powder in the left column, coarser powder in the central column, and raw powder on the right. Higher magnification of cleavage and dimples.

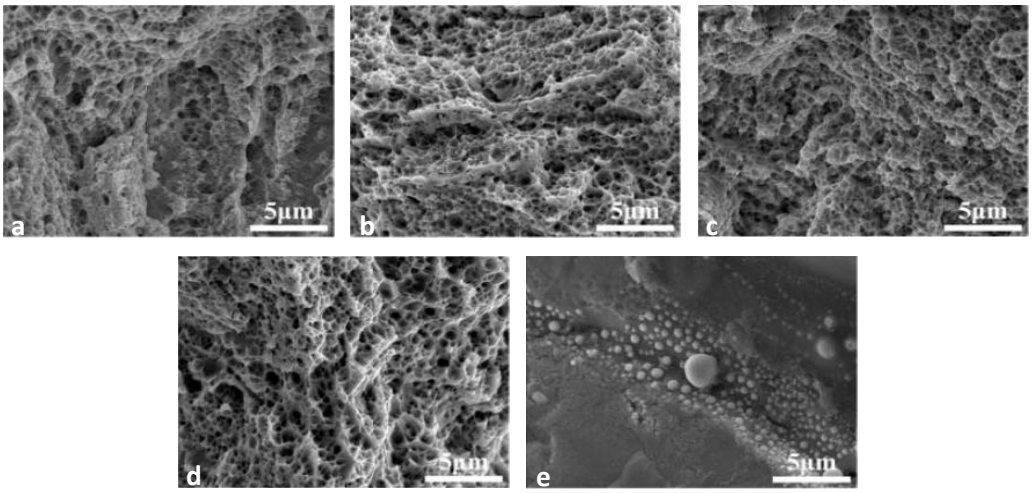

Figure 3.13 SEM micrographs of fracture surface of samples with tilt angle of 0°, 30°, 45°, 60°, 90° from *a* to *e*.

3.5 Surface roughness

Surface properties are widely investigated due to the remarkable role played in engineering applications. It is mandatory to know the roughness of as-built components to evaluate the need for further machining operations. A generical hot-rolled 316L is considered as a conventionally manufactured component for comparison; the surface roughness, in that case, is around 2 – 4 μm [85]. As shown in Table 3.3 below, the LPBF produces samples with a rougher surface, not suitable for many technical uses. The comparison between gas and water atomized powder as feedstock material can be carried out also from the surface roughness point of view [35]. Water atomized powder produces components with higher surface roughness than gas atomized powder.

Table 3.3 Surface roughness values collected in literature.

Surface roughness (μm)	Reference
12	[86]
12.4	[87]
9	[60]
6.1	[88]
10	[89]
5	[68]
4.79	[88]
7.69	[61]
14	[90]
12.44	[91]
8.72	[92]
8.04	[48]
11	[75]
136	[51]
15	[38]
8.8	[93]
10	[29]
9.3	[94]

In some cases, the remelting is a good strategy for producing a smoother surface. This process consists of a second scan with laser on already solidified material and carries out only on the top layer. Otherwise, the second scan after each layer is an additional option that allows for a higher relative density [87,95]. The effect of VED on surface finishing shows the same trend previously discussed for the density; as the VED rises as the surface roughness decrease until an optimal range in which surface roughness is constant, further increase of VED value is detrimental for surface finishing [60]. Wang et al. [88] confirmed this tendency and stated that the optimal range of VED for optimizing surface roughness does not overlap with the one that maximizes density. The surface roughness is influenced in a significant way by the layer thickness and tilting angle. Indeed, as Shi et al. [51] reported, superior layer thickness leads to higher surface roughness. Significant results are reported by Wang et al. [96] for overhang structure, who report an increase of surface roughness when the tilting angle of the surface decreases both for the upper and lower surface. The surface roughness values for the upper and lower surfaces are similar for high angles, whereas the tilting ones reduce the surface roughness values for the upper and lower surface become different, the upper surface has a better surface finishing.

3.6. Cost analysis

An analysis on the comparison between gas and water atomized powder requires also study production costs. The following survey evaluates the price and how a specific type of feedstock material impacts the global production cost. The latter consists of two parts; the first one is related to machine cost (C_j), while the second is to material's one. The former is composed of the amortization of machine price, the cost of energy used, and

the atmosphere gas, as shown in Equation 3.2. Design costs are not considered as it can be hard to estimate the design process generally. Amortization is calculated as an average life span of 5 years (L_s) with an average of 5000 hours per year of use (H_y); once given the price of the machine (M_p) is possible to calculate the cost per hour. The global electrical power charge can be assessed by knowing the power consumption (P_u) and the price for a unit of power (P_c), in the same way knowing the gas flow (G_f) and gas cost (G_c) is possible to calculate the total gas cost.

$$C_j = \frac{M_p}{L_s * H_y} + G_f * G_c + P_u * P_c \tag{3.2}$$

The second addend for the total cost can be estimated by the amount of feedstock material needed and its price. Material cost is considered as price per unit hour, so to have a consistent result with the one relative to machine charge, the formula is reported in Equation 3.3. The global material cost is composed of component volume (V), density (ρ, which is considered 7.9×10^3 kg/m^3), powder cost (p), and two coefficients to evaluate support presence and reusability of unused feedstock material (k_s and k_r respectively). The cycle time is composed of the time required to perform the scanning and the time needed for the spreading of the powder bed after each layer melt. The first component can be calculated by dividing the component volume (V) by the build rate of the machine (B_r), the second one is obtained by the total number of layers (total height, H, divided by layer thickness, L_t) multiplied by the time of recoating (R_t), which is generally 8 seconds.

$$C_m = \frac{V * \rho * p * k_s * k_t}{\frac{V}{B_r} + \frac{H}{L_t} * R_t} \tag{3.3}$$

In this case, all parameters will be set on a 316L component produced by an EOS M290 with its recommended process parameters [97]. The component has a volume of 2×10^4 mm^3 with a height of 50 mm. Therefore, it is possible to calculate the global cost. Although this calculation is based on hypothetical components and is made to provide an idea of costs, they can vary considerably when using different machines or building other components. The crucial concept is that material cost has a slight impact on global cost. Table 3.4 summarizes the values used in the cost calculation.

Table 3.4 Parameters used for cost calculation.

Parameter		Value	Ref
Machine price (M_p)	€	5.74×10^5	[97]
Life span (L_s)	years	5	hyp.
Yearly use (H_y)	h/year	5×10^3	hyp.
Power consumption (P_u)	kW	2.4	[97]
Power cost (P_c)	€/kWh	2.23×10^{-1}	[98]
Gas flow (G_f)	m^3/h	1.5×10^{-1}	[97]
Gas cost (G_c)	€/m^3	3.23	[99]
Component volume (V)	mm^3	2×10^4	hyp.
Density (ρ)	kg/m^3	7.9×10^3	
GA powder cost (p)	€/kg	38	[100]
WA powder cost (p)	€/kg	26	[101]
Support factor (k_s)		1.25	hyp.
Recycle factor (k_r)		4	hyp.

Build rate (B_r)	mm^3/h	7.2×10^3	[97]
Component height (H)	mm	50	hyp.
Layer thickness (Lt)	μ	25	[97]
Recoating time (Rt)	s	8	[97]

This brief cost analysis provides a cost per hour of 28.1 euros per hour when using gas atomized powder; while using water atomized powder, the cost is 26.8 euros per hour. This slight difference is the result of the different costs of the two types of powder. Results allow us to deduce that the costs are lower when using water atomized powders, but a more complex analysis is required. It is also mandatory to evaluate the mechanical properties and other features that can be affected by the feedstock material. According to the literature, the gas atomized powder is the best choice due to the better properties achievable, whereas the drawback of higher cost can be neglected.

4. Material and methods

4.1 Feedstock material

The experimental process consists of different steps; the first is the production of cubic samples used to evaluate the dimensional accuracy, the relative density, and the surface roughness. The cubic samples are produced varying some process parameters in order to investigate their effects. Subsequently, some tensile samples are produced and then tested to study the tensile properties.

The feedstock materials used are two types of powder, one gas atomized powder from EOS [100] and one water atomized powder from Pometon [101]. The chemical composition is reported in Table 4.1. Both types of powder have a granulometric distribution in the range between 15 – 50 μm.

Table 4.1 Chemical composition of the AISI 316L powders, provided by the manufacturers [wt%].

Element	**GA by EOS** [100]	**WA by Pometon** [101]
Fe	Balance	Balance
Cr	17 - 19	16.5 – 18.5
Ni	13 - 15	10 – 13
Mo	2.25 – 3	2 – 2.5
C	0.03	< 0.03
N	0.10	< 0.11
Mn		< 2

Before loading the feedstock material in the machine, the raw material was treated in an oven for one hour at 80°C. In this way, it is possible to operate the degassing and introduce the powder with the desired chemical composition.

4.2 Design of experiment

The additive manufacturing machine employed in this work is Mlab cusing R by GE Additive, Figure 4.2. Figure 4.1 below shows the interior of the building chamber. Samples produced are 16 cubes with a nominal dimension of 12 × 12 × 12 mm^3. The first job was built with gas atomized powder, while in the second, the feedstock material was water atomized powder following the same DoE reported in Table 4.2. The laser employed has a maximum power output of 100 W. The focus of the beam is around 50 μm. The first target of this work is the evaluation of the density of samples. As can be noticed, four scanning speeds (Ss) are selected (very low: SSVL; low: SSL; high: SSH; very high: SSVH), while hatch spacing (Hs) differs in a range of five values (very low: HDVL; low: HDL; medium: HDM; high: HDH; very high: HDVH). Table 2 does not report the layer thickness (Lt) value, kept constant at 25 μm, and the laser power (Lp) sets at 95 W. As shown in the table, the VED is different for each sample as its value is the result of all other process parameters. According to Equation (3.1), the VED varies in the range 56.5 and 99.0 J/mm^3. Nevertheless, samples from numbers 1 to 8 have the same process parameters as samples 9 to 16. However, they differ in the scanning strategy: in the first half of the samples, the laser path follows a chessboard pattern, as shown in Figure 4.3a, in the second half, the scanning strategy is stripy with a rotation between each successive layer of 67°, shown in Figure 4.3b and 4.3c.

Table 4.2 Design of Experiment used for building density samples.

Sample	Ss (mm/s)	Hs (µm)	VED (J/mm^3)	Scanning strategy
1	SSVL	HSM	90.5	Chess / Meander
2	SSL	HSM	75.4	
3	SSH	HSM	64.6	
4	SSVH	HSM	56.5	
5	SSL	HSVL	99.0	
6	SSL	HSL	85.6	
7	SSL	HSH	67.4	
8	SSL	HSVH	60.9	
9	SSVL	HSM	90.5	Stripe / 67
10	SSL	HSM	75.4	
11	SSH	HSM	64.6	
12	SSVH	HSM	56.5	
13	SSL	HSVL	99.0	
14	SSL	HSL	85.6	
15	SSL	HSH	67.4	
16	SSL	HSVH	60.9	

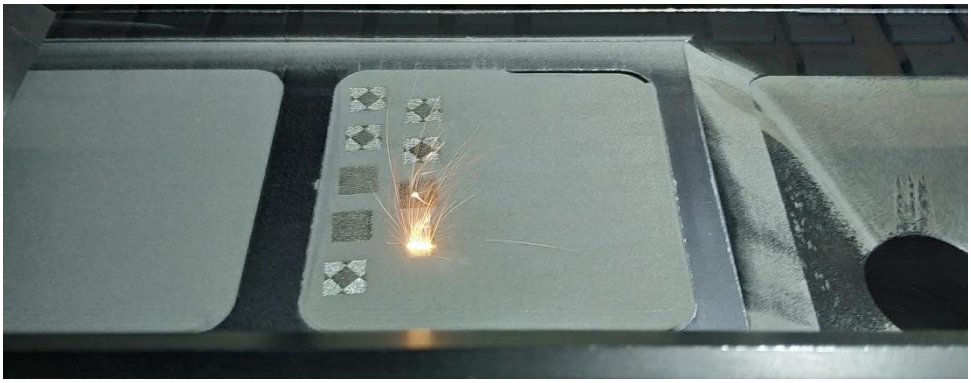

Figure 4.1 Building chamber of Mlab cusing R used for samples production. On the left, there is the feedstock material. In the central zone can be noticed the presence of sparks due to the laser effect on powders.

Figure 4.2 Mlab cusing R machine used for the production of all parts in this work [102].

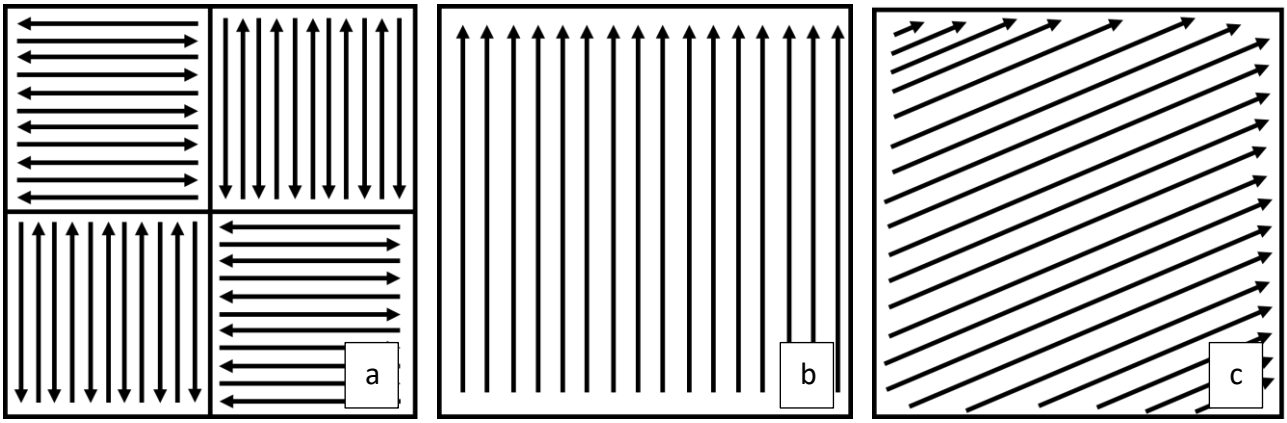

Figure 4.3 Chess/meander scanning strategy (a). Stripe/67 scanning strategy on two successive layers (b and c).

Figure 4.4 below proves how the top surface can change employed two different scanning strategies. A chessboard and edges between two domains are noticeable on the left, while on the right, no borders are visible due to the stripe scanning strategy.

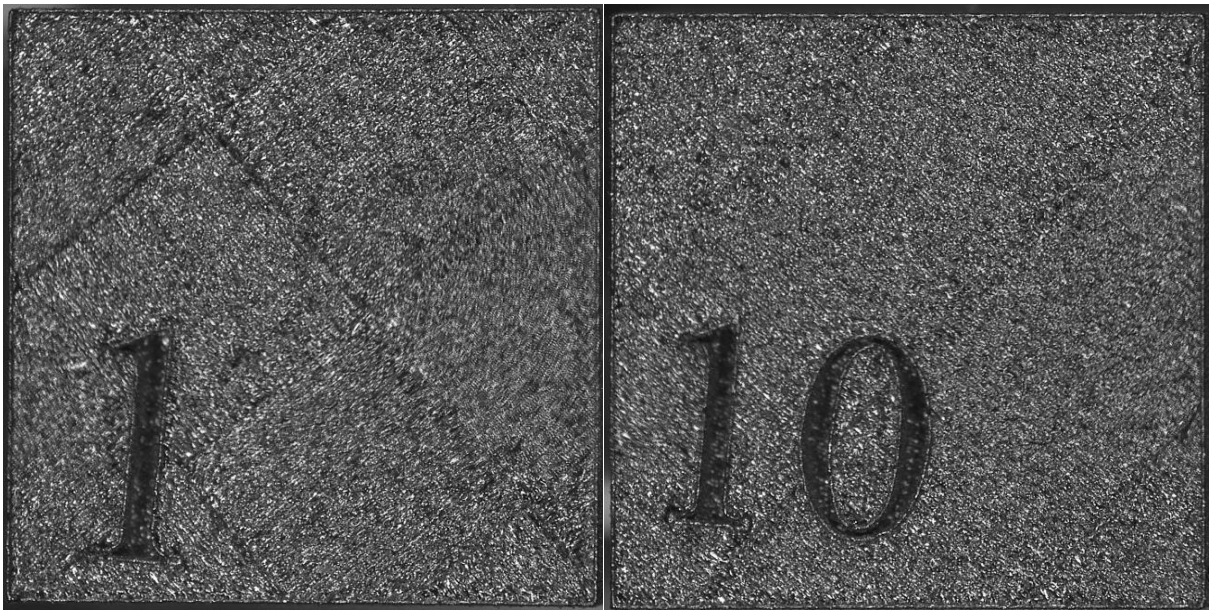

Figure 4.4 Top surface of two gas atomized samples. On the right sample number 10, on the left number 01.

4.3 Testing methods

The first step is the density measurement. The cubes are removed from the building platform through an EDM wire cutting machine. The cubes obtained are then dry weighed to know precisely the mass of the sample. Subsequently, the specimen was dipped in water to measure the weight, which is different from the dry one due to the Archimede principle. The difference is the weight of the water that occupies the volume of the sample. The setup used to measure the weight of samples is reported in Figure 4.5.

Figure 4.5 Weight scale used in density measurements.

As explained in the Equations (4.1 - 4.3) below, it is possible to evaluate the relative density.

$$V_{sample} = \frac{(m_{dry} - m_{dip})}{\rho_{H_2O}} \quad (4.1)$$

In this way, it is possible to evaluate the density of the sample simply by knowing the volume from Equation (4.1) and the dry mass using Equation (4.2).

$$\rho_{sample} = m_{dry} / V_{Sample} \quad (4.2)$$

Once the density of the sample is known, it is possible to calculate the relative density using Equation (4.3) below.

$$Relative\ density = \rho_{sample} / \rho_{theoretical} \quad (4.3)$$

The measurement has been repeated three times per sample to achieve better accuracy of the density value. Subsequently, the cubes are measured with a caliber to estimate the dimensional accuracy obtained through the process.

The surface roughness measurement was performed with a profilometer RTP 80 shown in Figure 4.6. The data are collected from the top surface and lateral surfaces, the lower surface, which was in contact with the building platform, is not considered in this analysis. Three measurements were made from every surface to collect Ra and Rz values. As a result, one roughness profile is acquired for each cube side. The process has been conducted according to the ISO 4287, setting a cutoff length of 0.8 mm and a cutoff number of 5.

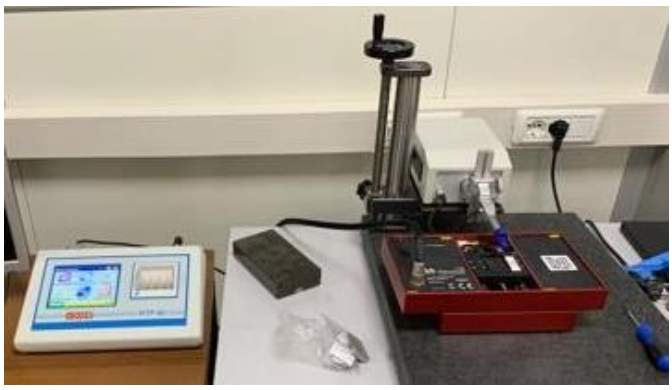

Figure 4.6 Profilometer RTP 80 by SM Instruments [103].

The tensile specimens produced are five with gas atomized powder and three samples using water atomized one. The tensile test was performed at room temperature, and the speed of strain was set constant at 2 mm/min.

5. Results and discussion

5.1 Dimensional accuracy

The first part of the analysis concerns dimensional accuracy. The samples are measured with a caliber three times, and then the average value is considered. As reported in Table 5.1, the GA samples result in higher dimensional accuracy and lower standard deviation

Table 5.1 Dimensional accuracy of all samples.

	GA		**WA**	
Sample	**Average dimension [mm]**	**St.Dev**	**Average dimension [mm]**	**St.Dev**
1	12.00	0.00	12.00	0.00
2	12.02	0.02	12.02	0.02
3	12.03	0.02	12.05	0.00
4	12.03	0.02	12.05	0.04
5	12.02	0.02	12.02	0.02
6	12.00	0.00	12.02	0.02
7	12.00	0.00	12.03	0.02
8	12.02	0.02	12.05	0.00
9	12.00	0.00	12.02	0.02
10	12.00	0.00	12.03	0.02
11	12.00	0.00	12.03	0.02
12	12.05	0.00	12.07	0.02
13	12.02	0.02	12.03	0.02
14	12.02	0.02	12.03	0.02
15	12.03	0.02	12.05	0.00
16	12.03	0.02	12.08	0.02
Mean	12.02	0.02	12.04	0.02

5.2 Density

Table 5.2 collects the density outcomes. As can be evaluated from the values reported, the water atomized powder produced samples with a lower density than gas atomized powder. The latter phenomenon is confirmed in literature as Lavery et al. [32] stated that water atomized powder shows a lower flowability. Furthermore, as Strondl et al. [31] discussed, the lower flowability leads to a lower pack density of powder bed and, consequently, a lower density of built part.

Table 5.2 The relative density of samples produced with gas atomized powder on the left, while the relative density of samples built using water atomized powder on the right side.

Sample	Relative Density (%)	Sample	Relative Density (%)
GA01	99.41	WA01	97.17
GA02	99.29	WA02	97.65
GA03	98.71	WA03	97.07
GA04	96.67	WA04	96.13
GA05	99.39	WA05	96.62
GA06	99.29	WA06	98.11
GA07	98.79	WA07	98.13
GA08	96.48	WA08	95.65
GA09	99.48	WA09	99.02
GA10	99.40	WA10	98.35
GA11	99.12	WA11	97.86
GA12	97.62	WA12	97.18
GA13	99.52	WA13	96.29
GA14	99.63	WA14	97.12
GA15	99.46	WA15	98.11
GA16	97.87	WA16	97.58

In Figure 5.1 below, there is a graphic representation of the data in Table 5.2. The process parameters set in the building of GA and WA samples are equal. Consequentially GA powders can reach a higher relative density. The GA14 achieved the maximum value among the GA ones, setting the Stripe/67 scanning strategy, a low scanning speed (SSL), and a low hatch spacing (HSL). However, through the latter set, the highest density for water atomized powder is not allowed. For this reason, the process parameter optimization outcomes for both powder types do not correspond. Indeed, the densest WA sample was the WA09 produced with Stripe/67 scanning strategy, very low scanning speed (SSVL), and the medium hatch spacing (HSM).

Nevertheless, the density data collected agree with the results reported in the literature. Although, as stated by Greco et al. [93], the density reached in their work is around 95.7% produced with a VED of 119 J/mm^3, a higher value compared to the ones in Table 4, the difference in density reported can be the effect of the non-appropriate ratio of process parameters [17]. Another source [27] claims that the density can be raised above 99.9% with a particular set of process parameters (laser power 400W, scanning speed 200 mm/s, hatch spacing 45 μm, and layer thickness 200 μm) using GA powder.

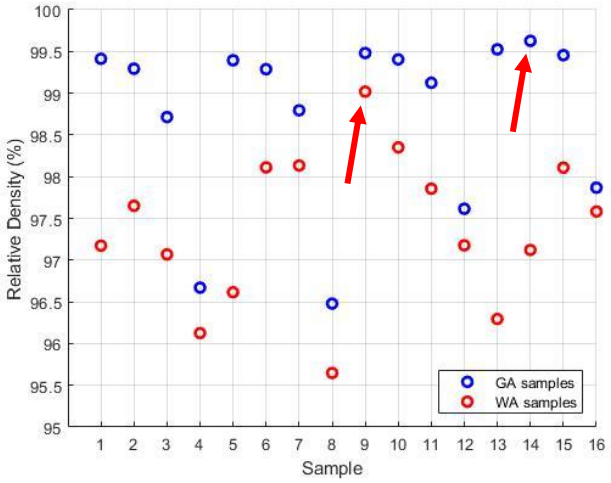

Figure 5.1 Plot of relative density for all samples produced. The arrows show the densest sample for each type of feedstock material.

Beyond the feedstock influence on density, the VED fluctuation can affect the porosity. Indeed, Figure 5.2 illustrates the outcomes highlighting the difference between GA and WA samples blue and red markers, and the Chess/Meander and the Stripe/67 scanning strategy, respectively marked with circles and triangles. The GA samples show an increase of relative density in the range of 60 J/mm^3 and 65 J/mm^3. The porosity content is more or less constant for higher VED values, as confirmed in literature [43]. However, the trend of the WA samples is slightly different. Precisely, there is a density growth similar to the case of GA samples at lower VED, but there is also a decrease of density at higher VED. In addition, the scanning strategy influence is remarkable, because in most cases, the Stripe/67 strategy produces samples with a higher density.

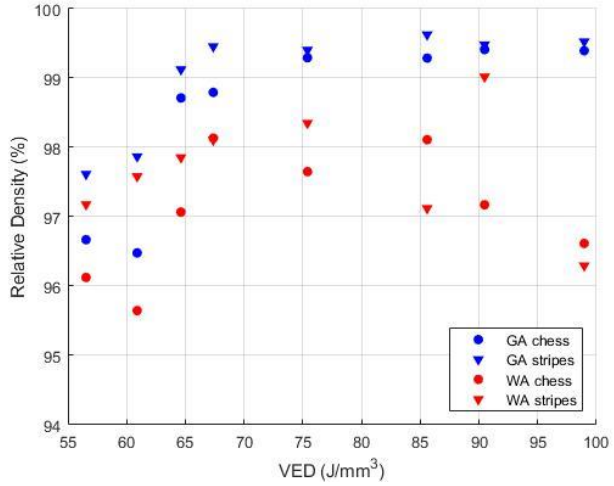

Figure 5.2 Density as a function of VED.

Scanning speed and hatch spacing can affect in different ways the density of parts, as shown in Figure 5.3. As the speed increases, the density decreases, especially for the WA samples. Indeed, the density of GA samples has a constant trend at low hatch spacing values while it drops at higher ones. The WA density shows the highest value from HSM to HSH but decreases at lower and higher hatch spacing.

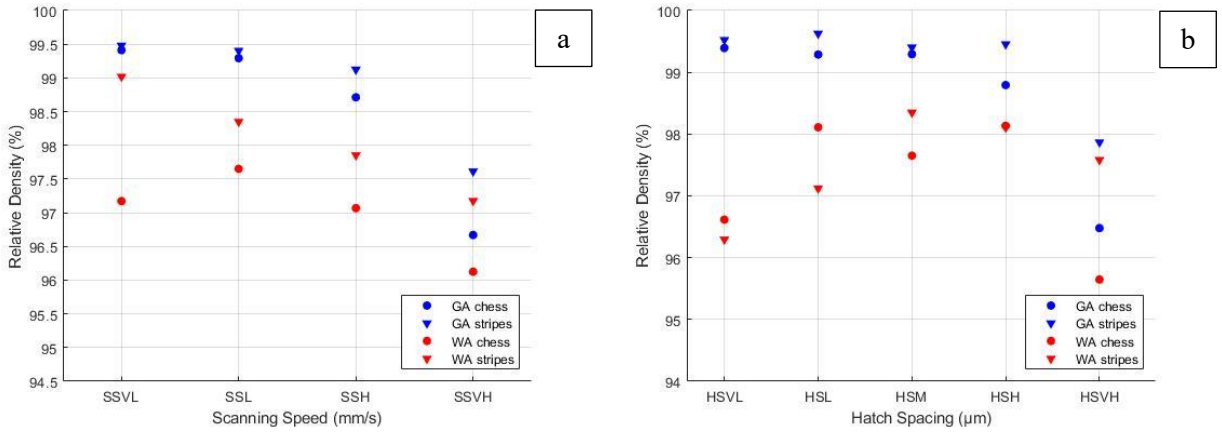

Figure 5.3 Relative density as a function of (a) scanning speed and (b) hatch spacing.

As already reported, high relative density implies better mechanical properties. As mentioned in Table 5.2, the density is maximized with two different sets of process parameters. Nevertheless, for the production of the tensile samples, the same set of process parameters is used for both types of powder. The scanning strategy adopted is Stripe/67, the low scanning speed (SSL), and low hatch spacing (HSL).

5.3 Surface roughness

The surface roughness is an essential feature of the LPBF process, and it is widely investigated in the literature. Generally, the surface roughness is included in the range between 7 – 15 µm [61,89–91]. Some authors claim that it is possible to reach a surface roughness of 2 µm [105]. The first important feature to analyze is the effect of powder used on the surface roughness. Figure 5.4a is reported the surface roughness as a function of VED for the top surface. The samples produced with gas atomized powder generally have a lower surface roughness when compared with samples produced with water atomized powder. The latter trend is widely confirmed in the range of higher VED, in which the GA samples show a decrease of surface roughness with a minimum peak at 85.6 J/mm3. In the range of lower VED, the two types of samples can be considered with the same surface roughness. As stated before, the GA samples improve the surface smoothness when increasing the VED, while WA samples increase their surface roughness when increasing the VED. According to the results, it would not be possible to achieve the lowest possible surface roughness for both water and gas atomized powder using the same set of process parameters. The lowest surface roughness achieved on the top surface is sample number 6 for gas atomized powder, with a surface roughness of 7.89 µm, and the number 12 for water atomized powder with 10.59 µm.

The surface roughness has also been measured on the lateral surfaces, and the results are collected in Figure 5.4b. In this case, both GA and WA samples show the same trend as a function of VED, and the surface roughness decreases slightly as VED increase. The main difference when comparing the top surface with the lateral one is that, in the latter case, the WA samples have a lower surface roughness than GA samples. However, it is also possible to notice that the lateral surface has a smoother surface when compared with the top surface.

The difference in surface roughness between lateral and top surfaces is a well-known phenomenon in literature [92,106]. The surface roughness appears to be lower on the top surface and higher on the lateral surfaces. Conversely, as reported in Figures 5.4 – 5.5, the lateral surface shows a lower surface roughness. Figure 5.5 shows the roughness profile. It is visible as the blue line, which represents the lateral surface, has lower and tighter peaks than the red line.

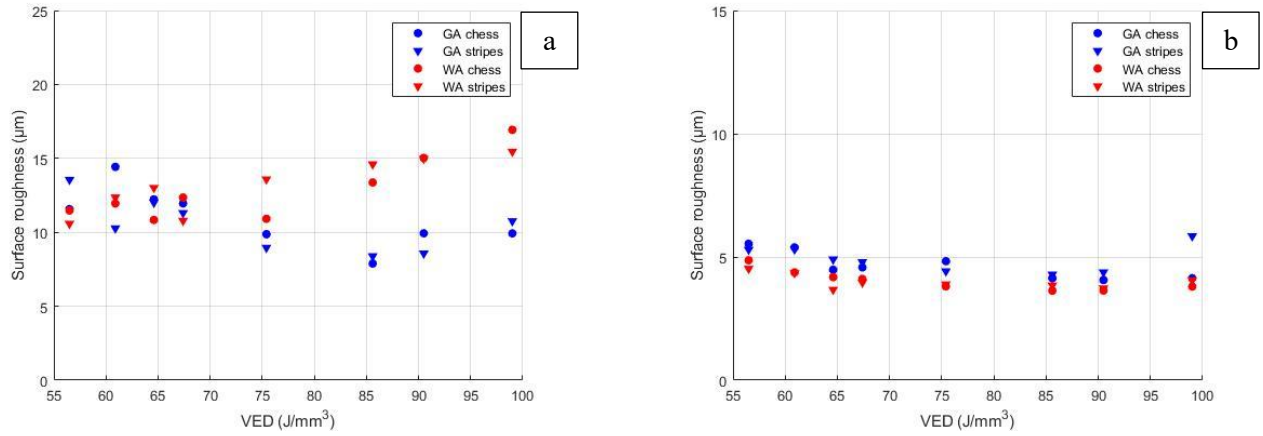

Figure 5.4 Surface roughness as a function of VED for (a) top surface and (b) lateral surface.

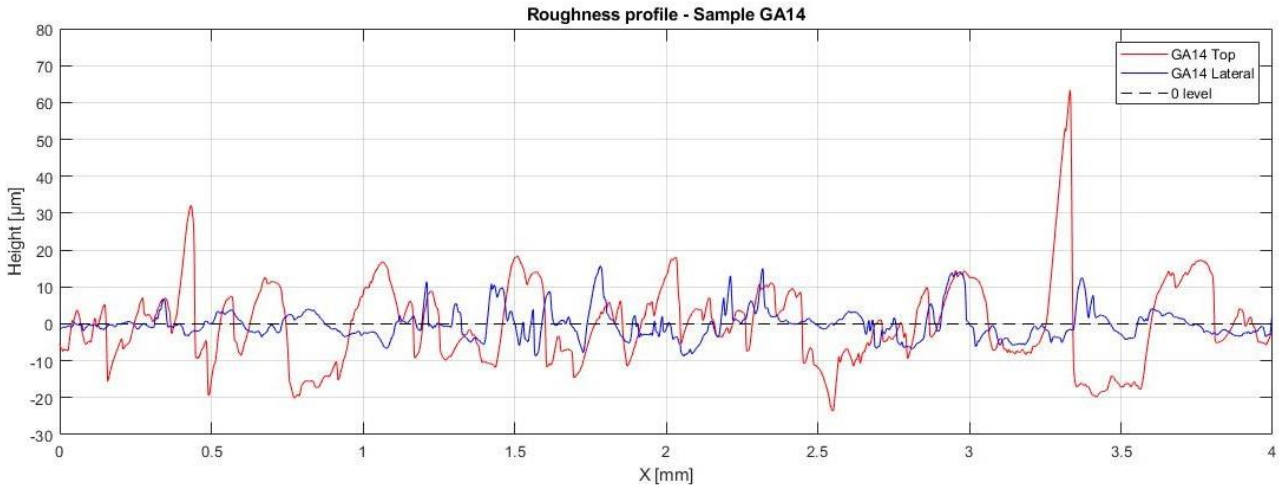

Figure 5.5 Roughness profile of two different surfaces of GA14 sample

The feedstock material is not the only parameter that can affect the surface roughness in the SLM process. Indeed, as seen before, also VED influences the built component. During the production of the samples, two parameters were varied, scanning speed and hatch spacing, and both influenced the surface roughness. As shown in Figure 5.6b, the effect of hatch spacing is similar on two types of feedstock material. There is a minimum peak in both cases, but in correspondence with two different scanning speed values, WA samples achieve the lowest surface roughness at high hatch spacing (HSH) while GA samples show their peak low hatch spacing (HSL). Scanning speed affects the surface roughness oppositely. For example, increased laser focus speed increased surface roughness in gas atomized powder's case using water atomized powder. However, the effect is the opposite, as reported in Figure 5.6a.

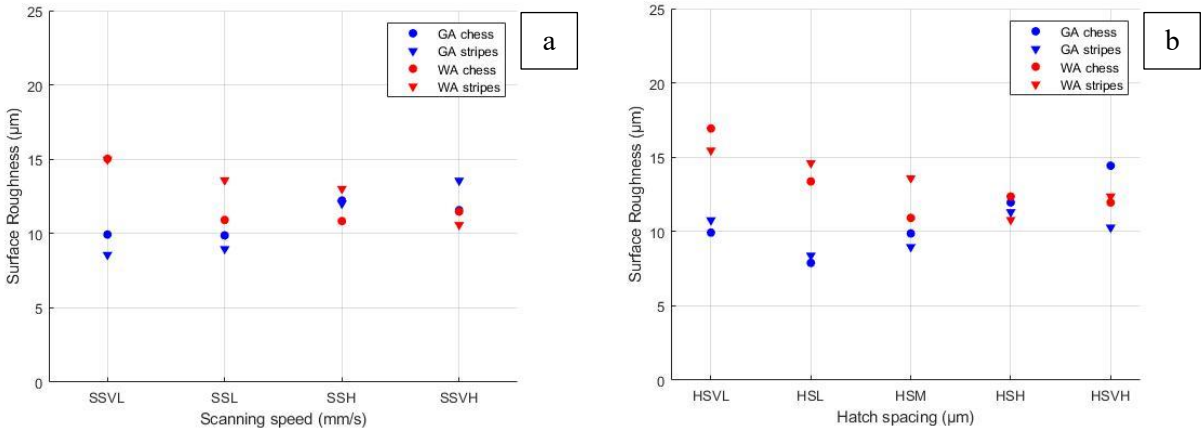

Figure 5.6 Surface roughness as a function of (a) hatch spacing and (b) scanning speed.

5.4 Mechanical properties

In the present work, mechanical properties are the last step of the analysis. As already reported, the optimized process parameters used to produce tensile samples are the ones that maximize the density of gas atomized samples. The tensile tests are performed with tensile testing machinery. The tensile samples produced are 8; five are made with gas atomized powder, while the rest are made with water atomized powder. The samples were produced horizontally on the building platform. This orientation provides better mechanical properties than vertical orientation because the stress is oriented in the same direction of each layer and not across different layers [69].

The tensile test results are reported in Table 5.3 below. The central aspect of this work consists of the comparison between the two types of feedstock material. It is possible to notice the first big difference when comparing the yield strength obtained; indeed, the gas atomized samples almost reach 540 MPa (sample 3), while the minimum achieved is around 505 MPa (sample 5). On the other hand, the water atomized samples cannot reach those yield strength levels, but rather, they attest in the range between 460 – 480 MPa. The values obtained for 316L gas atomized powder samples find confirmation in the literature as Liu et al. [27] reports that in their work, yield strength achieved with several sets of process parameters ranged between 423 and 530 MPa. Thus, the ultimate tensile strength reaches the mean values found in the literature, and, according to what is shown for the yield strength, the water atomized samples achieve lower values than gas atomized samples. As can be noticed in Figure 5.7, the different feedstock material also affects the elongation of samples. Indeed, the gas atomized powder show a more prominent elongation at failure. This behavior is confirmed by Riabov et al. [36]; in their work, the gas atomized powder produced samples with higher yield strength and elongation at break.

Table 5.3 Mechanical test results. Yield strength (YS), ultimate tensile strength (UTS), elongation at maximum stress (ε), elongation at failure (ε_f)

Sample	YS [MPa]	UTS [MPa]	ε (%)	ε_f (%)
GA01	522.9	617.6	17.76	24.34
GA02	516.2	611.4	17.08	24.83
GA03	539.5	614.9	18.38	25.49
GA04	517.6	608.6	18.81	27.03
GA05	506.2	599.8	18.74	25.82

WA01	464.6	576.5	21.15	22.63
WA02	480.2	596	18.2	19.57
WA03	464.4	573.3	19.31	20.16

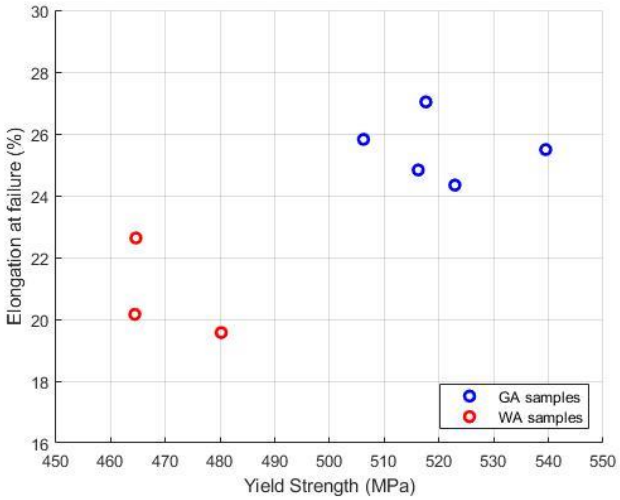

Figure 5.7 Elongation at failure as function of yield strength.

Another essential difference between the two types of samples is the behavior after reaching the ultimate tensile strength. Indeed, the GA samples show a lower elongation (ε) than WA samples, but the latter has a short necking zone in which the elongation continues for less than 2%. On the other hand, oppositely, gas atomized samples continue the deformation for more than 6%, reaching an elongation at failure higher than the water atomized samples.

6. Conclusions

In this last paragraph, all the previous results are briefly summarized. This work aimed to highlight the differences of the process and the properties of the final component when using gas or water atomized powder. The state of art investigation gave prominence to various aspects related to the process. The first feature is the feedstock material effect on powder bed formation, in particular, how the spherical shape of GA powder can produce a more homogeneous and packed powder bed. Another process-related feature is the cost evaluation; the result of the calculation proves how the LPBF process is 5% cheaper using WA powder instead of GA powder. The product-related features are surface roughness and mechanical properties. The analysis of tensile properties data available in literature shows how the yield strength is comparable between the two types of feedstock material. The main difference is the lower elongation at break of WA tensile samples. Various sources agree that GA powder produces parts with a lower surface roughness than water atomized powder.

The dimensional accuracy analysis provided better results in gas atomized samples. The density is generally higher in gas atomized samples, but the peak density is reached with two different sets of process parameters. The different density is the result of the differences in powder bed formation. Generally, WA powder produces a less dense powder bed than GA powder. The different powder morphology can originate the cause of this effect; the irregular shape of the WA powder creates pores in the powder bed, these pores generate porosity in the final component. As noticed in the Increasing VED produces an increase of densification in both cases of feedstock material. However, in the water atomized samples case, a peak and a subsequent decrease are noticed after increasing density. The latter effect can be explained by the production of key-hole defects when using a higher VED. Oppositely, using a lower VED leads to a lower density due to the lack of fusion.

The surface roughness shows two different trends and values when considering the top and lateral surfaces; the latter shows a smoother surface. Although the surface roughness is comparable between the two types of feedstock material at lower VED when considering only the top surface, increasing the energy provided to melt pool the gas atomized samples show a decrease in roughness, while water atomized samples increase their surface roughness. On the other hand, the water atomized samples show a lower surface roughness at any VED value on the lateral surface. As can be seen, by the results, it is impossible to optimize density and surface roughness with the same set of process parameters.

For what concerns the mechanical properties, the gas atomized powder allowed samples with higher yield strength. Indeed, according to the results, the average yield strength of GA samples is about 10% higher than WA samples. On the other hand, the average elongation at failure showed by samples produced with water atomized samples is 21% lower with respect to samples produced with gas atomized powder. Another critical difference is the behavior between the two types of samples is the part after reaching the ultimate tensile strength. Indeed, the GA samples continue the deformation while WA samples arrive at failure with a lower elongation. As reported in the density results section, the GA samples achieve higher densities with the selected process parameters. Thus, the GA tensile samples are denser than the WA ones. For this reason, the difference between the two types of samples can be explained.

7. Bibliography

[1] M. Bici, S. Brischetto, F. Campana, C.G. Ferro, C. Seclì, S. Varetti, P. Maggiore, A. Mazza, Development of a multifunctional panel for aerospace use through SLM additive manufacturing, Procedia CIRP. 67 (2018) 215–220. https://doi.org/10.1016/j.procir.2017.12.202.

[2] M. Yakout, M.A. Elbestawi, S.C. Veldhuis, S. Nangle-Smith, Influence of thermal properties on residual stresses in SLM of aerospace alloys, Rapid Prototyp. J. 26 (2020) 213–222. https://doi.org/10.1108/RPJ-03-2019-0065.

[3] J. Yu, D. Kim, K. Ha, J.B. Jeon, W. Lee, Strong feature size dependence of tensile properties and its microstructural origin in selectively laser melted 316L stainless steel, Mater. Lett. 275 (2020) 128161. https://doi.org/10.1016/j.matlet.2020.128161.

[4] R. Leal, F.M. Barreiros, L. Alves, F. Romeiro, J.C. Vasco, M. Santos, C. Marto, Additive manufacturing tooling for the automotive industry, Int. J. Adv. Manuf. Technol. 92 (2017) 1671–1676. https://doi.org/10.1007/s00170-017-0239-8.

[5] C.M. González-Henríquez, M.A. Sarabia-Vallejos, J.R. Hernandez, Antimicrobial polymers for additive manufacturing, Int. J. Mol. Sci. 20 (2019). https://doi.org/10.3390/ijms20051210.

[6] M.B. Canciglieri, A.F.C.S. de M. Leite, A.L. Szejka, O. Canciglieri Júnior, An approach for dental prosthesis design and manufacturing through rapid manufacturing technologies, Int. J. Comput. Integr. Manuf. 32 (2019) 832–847. https://doi.org/10.1080/0951192X.2019.1636410.

[7] M.H. Mosallanejad, B. Niroumand, A. Aversa, A. Saboori, In-situ alloying in laser-based additive manufacturing processes: A critical review, J. Alloys Compd. 872 (2021) 159567. https://doi.org/https://doi.org/10.1016/j.jallcom.2021.159567.

[8] A. Aversa, A. Saboori, E. Librera, M. [de Chirico], S. Biamino, M. Lombardi, P. Fino, The Role of Directed Energy Deposition Atmosphere Mode on the Microstructure and Mechanical Properties of 316L Samples, Addit. Manuf. (2020) 101274. https://doi.org/https://doi.org/10.1016/j.addma.2020.101274.

[9] A. Saboori, D. Gallo, S. Biamino, P. Fino, M. Lombardi, An overview of additive manufacturing of titanium components by directed energy deposition: Microstructure and mechanical properties, Appl. Sci. 7 (2017). https://doi.org/10.3390/app7090883.

[10] A. Röttger, J. Boes, W. Theisen, M. Thiele, C. Esen, A. Edelmann, R. Hellmann, Microstructure and mechanical properties of 316L austenitic stainless steel processed by different SLM devices, Int. J. Adv. Manuf. Technol. 108 (2020) 769–783. https://doi.org/10.1007/s00170-020-05371-1.

[11] A. Saboori, A. Aversa, G. Marchese, S. Biamino, M. Lombardi, P. Fino, Microstructure and mechanical properties of AISI 316L produced by directed energy deposition-based additive manufacturing: A review, Appl. Sci. 10 (2020). https://doi.org/10.3390/app10093310.

[12] K.S. Derekar, A review of wire arc additive manufacturing and advances in wire arc additive manufacturing of aluminium, Mater. Sci. Technol. (United Kingdom). 34 (2018) 895–916. https://doi.org/10.1080/02670836.2018.1455012.

[13] A. Saboori, G. Piscopo, M. Lai, A. Salmi, S. Biamino, An investigation on the effect of deposition pattern on the microstructure, mechanical properties and residual stress of 316L produced by Directed Energy Deposition, Mater. Sci. Eng. A. 780 (2020) 139179. https://doi.org/https://doi.org/10.1016/j.msea.2020.139179.

[14] A. Saboori, A. Abdi, S.A. Fatemi, G. Marchese, S. Biamino, H. Mirzadeh, Hot deformation behavior

and flow stress modeling of Ti–6Al–4V alloy produced via electron beam melting additive manufacturing technology in single β-phase field, Mater. Sci. Eng. A. 792 (2020) 139822. https://doi.org/https://doi.org/10.1016/j.msea.2020.139822.

[15] M. Galati, L. Iuliano, A literature review of powder-based electron beam melting focusing on numerical simulations, Addit. Manuf. 19 (2018) 1–20. https://doi.org/10.1016/j.addma.2017.11.001.

[16] W. Zhai, Z. Zhu, W. Zhou, S.M.L. Nai, J. Wei, Selective laser melting of dispersed TiC particles strengthened 316L stainless steel, Compos. Part B Eng. 199 (2020) 108291. https://doi.org/10.1016/j.compositesb.2020.108291.

[17] S. Greco, K. Gutzeit, H. Hotz, B. Kirsch, J.C. Aurich, Selective laser melting (SLM) of AISI 316L—impact of laser power, layer thickness, and hatch spacing on roughness, density, and microhardness at constant input energy density, Int. J. Adv. Manuf. Technol. 108 (2020) 1551–1562. https://doi.org/10.1007/s00170-020-05510-8.

[18] J. Piekło, A. Garbacz-Klempka, Use of maraging steel 1.2709 for implementing parts of pressure mold devices with conformal cooling system, Materials (Basel). 13 (2020) 1–22. https://doi.org/10.3390/ma13235533.

[19] N. Kaleli, D. Saraç, Comparison of porcelain bond strength of different metal frameworks prepared by using conventional and recently introduced fabrication methods, J. Prosthet. Dent. 118 (2017) 76–82. https://doi.org/10.1016/j.prosdent.2016.12.002.

[20] L. Ventola, F. Robotti, M. Dialameh, F. Calignano, D. Manfredi, E. Chiavazzo, P. Asinari, Rough surfaces with enhanced heat transfer for electronics cooling by direct metal laser sintering, Int. J. Heat Mass Transf. 75 (2014) 58–74. https://doi.org/10.1016/j.ijheatmasstransfer.2014.03.037.

[21] H.B. Jasim, B.A. Farhan, Materials Today : Proceedings Practical analysis of direct metal laser sintering process, Mater. Today Proc. (2021). https://doi.org/10.1016/j.matpr.2021.02.138.

[22] M. Aristizabal, P. Jamshidi, A. Saboori, S.C. Cox, M.M. Attallah, Laser powder bed fusion of a Zr-alloy: Tensile properties and biocompatibility, Mater. Lett. 259 (2020) 126897. https://doi.org/https://doi.org/10.1016/j.matlet.2019.126897.

[23] F. Trevisan, F. Calignano, M. Lorusso, J. Pakkanen, A. Aversa, E.P. Ambrosio, M. Lombardi, P. Fino, D. Manfredi, On the selective laser melting (SLM) of the AlSi10Mg alloy: Process, microstructure, and mechanical properties, Materials (Basel). 10 (2017). https://doi.org/10.3390/ma10010076.

[24] A. V. Gusarov, S.N. Grigoriev, M.A. Volosova, Y.A. Melnik, A. Laskin, D. V. Kotoban, A.A. Okunkova, On productivity of laser additive manufacturing, J. Mater. Process. Technol. 261 (2018) 213–232. https://doi.org/10.1016/j.jmatprotec.2018.05.033.

[25] M. Aslam, F. Ahmad, P.S.M.B.M. Yusoff, K. Altaf, M.A. Omar, R. M.German, Powder injection molding of biocompatible stainless steel biodevices, Powder Technol. 295 (2016) 84–95.

[26] M. Lindgren, R. Suihkonen, J. Vuorinen, Erosive wear of various stainless steel grades used as impeller blade materials in high temperature aqueous slurry, Wear. 328–329 (2015) 391–400.

[27] Y. Liu, M. Zhang, W. Shi, Y. Ma, J. Yang, Study on performance optimization of 316L stainless steel parts by High-Efficiency Selective Laser Melting, Opt. Laser Technol. 138 (2021) 106872. https://doi.org/10.1016/j.optlastec.2020.106872.

[28] Q. Zeng, K. Gan, Y. Wang, Effect of Heat Treatment on Microstructures and Mechanical Behaviors of 316L Stainless Steels Synthesized by Selective Laser Melting, J. Mater. Eng. Perform. 30 (2021) 409–422. https://doi.org/10.1007/s11665-020-05330-7.

[29] R. Shrestha, J. Simsiriwong, N. Shamsaei, Fatigue behavior of additive manufactured 316L stainless steel under axial versus rotating-bending loading: Synergistic effects of stress gradient, surface roughness, and volumetric defects, Int. J. Fatigue. 144 (2021) 106063.

https://doi.org/10.1016/j.ijfatigue.2020.106063.

[30] C. Kim, H. Yin, A. Shmatok, B.C. Prorok, X. Lou, K.H. Matlack, Ultrasonic nondestructive evaluation of laser powder bed fusion 316L stainless steel, Addit. Manuf. 38 (2021) 101800. https://doi.org/10.1016/j.addma.2020.101800.

[31] A. Strondl, O. Lyckfeldt, H. Brodin, U. Ackelid, Characterization and Control of Powder Properties for Additive Manufacturing, Jom. 67 (2015) 549–554. https://doi.org/10.1007/s11837-015-1304-0.

[32] N.P. Lavery, J. Cherry, S. Mehmood, H. Davies, B. Girling, E. Sackett, S.G.R. Brown, J. Sienz, Effects of hot isostatic pressing on the elastic modulus and tensile properties of 316L parts made by powder bed laser fusion, Mater. Sci. Eng. A. 693 (2017) 186–213. https://doi.org/10.1016/j.msea.2017.03.100.

[33] P. Wang, A. Salandari-Rabori, Q. Dong, V. Fallah, Effect of input powder attributes on optimized processing and as-built tensile properties in laser powder bed fusion of AlSi10Mg alloy, J. Manuf. Process. 64 (2021) 633–647. https://doi.org/10.1016/j.jmapro.2021.02.024.

[34] P. Kiani, U. Scipioni Bertoli, A.D. Dupuy, K. Ma, J.M. Schoenung, A Statistical Analysis of Powder Flowability in Metal Additive Manufacturing, Adv. Eng. Mater. 22 (2020) 2000022--n/a.

[35] S. Hoeges, A. Zwiren, C. Schade, Additive manufacturing using water atomized steel powders, Met. Powder Rep. 72 (2017) 111–117. https://doi.org/10.1016/j.mprp.2017.01.004.

[36] D. Riabov, M. Rashidi, E. Hryha, S. Bengtsson, Effect of the powder feedstock on the oxide dispersion strengthening of 316L stainless steel produced by laser powder bed fusion, Mater. Charact. 169 (2020) 110582. https://doi.org/10.1016/j.matchar.2020.110582.

[37] J.J. Dunkley, Metal Powder Atomisation Methods for Modern Manufacturing, Johnson Matthey Technol. Rev. 63 (2019) 226–232.

[38] D. Zhang, J. Yu, H. Li, X. Zhou, C. Song, C. Zhang, S. Shen, L. Liu, C. Dai, Investigation of laser polishing of four selective laser melting alloy samples, Appl. Sci. 10 (2020). https://doi.org/10.3390/app10030760.

[39] S.M. Yusuf, E. Choo, N. Gao, Comparison between virgin and recycled 316l ss and alsi10mg powders used for laser powder bed fusion additive manufacturing, Metals (Basel). 10 (2020) 1–18. https://doi.org/10.3390/met10121625.

[40] L. Cordova, M. Campos, T. Tinga, Revealing the Effects of Powder Reuse for Selective Laser Melting by Powder Characterization, Jom. 71 (2019) 1062–1072. https://doi.org/10.1007/s11837-018-3305-2.

[41] H.P. Tang, M. Qian, N. Liu, X.Z. Zhang, G.Y. Yang, J. Wang, Effect of Powder Reuse Times on Additive Manufacturing of Ti-6Al-4V by Selective Electron Beam Melting, Jom. 67 (2015) 555–563. https://doi.org/10.1007/s11837-015-1300-4.

[42] C. Tian, X. Li, H. Li, G. Guo, L. Wang, Y. Rong, The effect of porosity on the mechanical property of metal-bonded diamond grinding wheel fabricated by selective laser melting (SLM), Mater. Sci. Eng. A. 743 (2019) 697–706. https://doi.org/10.1016/j.msea.2018.11.138.

[43] A. Leicht, M. Fischer, U. Klement, L. Nyborg, E. Hryha, Increasing the Productivity of Laser Powder Bed Fusion for Stainless Steel 316L through Increased Layer Thickness, J. Mater. Eng. Perform. 30 (2021) 575–584. https://doi.org/10.1007/s11665-020-05334-3.

[44] W.E. King, H.D. Barth, V.M. Castillo, G.F. Gallegos, J.W. Gibbs, D.E. Hahn, C. Kamath, A.M. Rubenchik, Observation of keyhole-mode laser melting in laser powder-bed fusion additive manufacturing, J. Mater. Process. Technol. 214 (2014) 2915–2925. https://doi.org/10.1016/j.jmatprotec.2014.06.005.

[45] W. Chen, G. Yin, Z. Feng, X. Liao, Effect of powder feedstock on microstructure and mechanical properties of the 316L stainless steel fabricated by selective laser melting, Metals (Basel). 8 (2018).

https://doi.org/10.3390/met8090729.

[46] M.L. Montero-Sistiaga, S. Pourbabak, J. Van Humbeeck, D. Schryvers, K. Vanmeensel, Microstructure and mechanical properties of Hastelloy X produced by HP-SLM (high power selective laser melting), Mater. Des. 165 (2019) 107598. https://doi.org/10.1016/j.matdes.2019.107598.

[47] P. Laakso, T. Riipinen, A. Laukkanen, T. Andersson, A. Jokinen, A. Revuelta, K. Ruusuvuori, Optimization and simulation of SLM process for high density H13 tool steel parts, Phys. Procedia. 83 (2016) 26–35. https://doi.org/10.1016/j.phpro.2016.08.004.

[48] Y. Deng, Z. Mao, N. Yang, X. Niu, X. Lu, Collaborative optimization of density and surface roughness of 316L stainless steel in selective laser melting, Materials (Basel). 13 (2020). https://doi.org/10.3390/ma13071601.

[49] Z. Dong, Y. Liu, W. Wen, J. Ge, J. Liang, Effect of hatch spacing on melt pool and as-built quality during selective laser melting of stainless steel: Modeling and experimental approaches, Materials (Basel). 12 (2018). https://doi.org/10.3390/ma12010050.

[50] Z. Sun, X. Tan, S.B. Tor, W.Y. Yeong, Selective laser melting of stainless steel 316L with low porosity and high build rates, Mater. Des. 104 (2016) 197–204. https://doi.org/10.1016/j.matdes.2016.05.035.

[51] W. Shi, P. Wang, Y. Liu, Y. Hou, G. Han, Properties of 316L formed by a 400 W power laser Selective Laser Melting with 250 μm layer thickness, Powder Technol. 360 (2020) 151–164. https://doi.org/10.1016/j.powtec.2019.09.059.

[52] J. Gubicza, M. El-Tahawy, Y. Huang, H. Choi, H. Choe, J.L. Lábár, T.G. Langdon, Microstructure, phase composition and hardness evolution in 316L stainless steel processed by high-pressure torsion, Mater. Sci. Eng. A. 657 (2016) 215–223. https://doi.org/10.1016/j.msea.2016.01.057.

[53] A. Röttger, K. Geenen, M. Windmann, F. Binner, W. Theisen, Comparison of microstructure and mechanical properties of 316 L austenitic steel processed by selective laser melting with hot-isostatic pressed and cast material, Mater. Sci. Eng. A. 678 (2016) 365–376. https://doi.org/10.1016/j.msea.2016.10.012.

[54] R. Casati, J. Lemke, M. Vedani, Microstructure and Fracture Behavior of 316L Austenitic Stainless Steel Produced by Selective Laser Melting, J. Mater. Sci. Technol. 32 (2016) 738–744. https://doi.org/10.1016/j.jmst.2016.06.016.

[55] A. Leicht, M. Rashidi, U. Klement, E. Hryha, Effect of process parameters on the microstructure, tensile strength and productivity of 316L parts produced by laser powder bed fusion, Mater. Charact. 159 (2020) 110016. https://doi.org/10.1016/j.matchar.2019.110016.

[56] J.P. Choi, G.H. Shin, M. Brochu, Y.J. Kim, S.S. Yang, K.T. Kim, D.Y. Yang, C.W. Lee, J.H. Yu, Densification behavior of 316L stainless steel parts fabricated by selective laser melting by variation in laser energy density, Mater. Trans. 57 (2016) 1952–1959. https://doi.org/10.2320/matertrans.M2016284.

[57] A. Habibiyan, A.Z. Hanzaki, H.R. Abedi, An investigation into microstructure and high-temperature mechanical properties of selective laser-melted 316L stainless steel toward the development of hybrid Ampliforge process, Int. J. Adv. Manuf. Technol. 110 (2020) 383–394. https://doi.org/10.1007/s00170-020-05870-1.

[58] E. Liverani, S. Toschi, L. Ceschini, A. Fortunato, Effect of selective laser melting (SLM) process parameters on microstructure and mechanical properties of 316L austenitic stainless steel, J. Mater. Process. Technol. 249 (2017) 255–263. https://doi.org/10.1016/j.jmatprotec.2017.05.042.

[59] W.M. Tucho, V.H. Lysne, H. Austbø, A. Sjolyst-Kverneland, V. Hansen, Investigation of effects of process parameters on microstructure and hardness of SLM manufactured SS316L, J. Alloys Compd. 740 (2018) 910–925. https://doi.org/10.1016/j.jallcom.2018.01.098.

[60] J.A. Cherry, H.M. Davies, S. Mehmood, N.P. Lavery, S.G.R. Brown, J. Sienz, Investigation into the effect of process parameters on microstructural and physical properties of 316L stainless steel parts by selective laser melting, Int. J. Adv. Manuf. Technol. 76 (2015) 869–879. https://doi.org/10.1007/s00170-014-6297-2.

[61] J. Hajnys, M. Pagac, O. Kotera, J. Petru, S. Scholz, Influence of basic process parameters on mechanical and internal properties of 316l steel in slm process for renishaw AM400, MM Sci. J. 2019 (2019) 2790–2794. https://doi.org/10.17973/MMSJ.2019_03_2018127.

[62] T. Kozior, J. Bochnia, P. Zmarzły, D. Gogolewski, Waviness of Freeform Surface Characterizations from, Materials (Basel). (2020).

[63] J. Gale, A. Achuhan, Application of ultrasonic peening during DMLS production of 316L stainless steel and its effect on material behavior, Rapid Prototyp. J. 23 (2017) 1185–1194. https://doi.org/10.1108/RPJ-09-2016-0140.

[64] K. Saeidi, X. Gao, F. Lofaj, L. Kvetková, Z.J. Shen, Transformation of austenite to duplex austenite-ferrite assembly in annealed stainless steel 316L consolidated by laser melting, J. Alloys Compd. 633 (2015) 463–469. https://doi.org/10.1016/j.jallcom.2015.01.249.

[65] B. Zhang, L. Dembinski, C. Coddet, The study of the laser parameters and environment variables effect on mechanical properties of high compact parts elaborated by selective laser melting 316L powder, Mater. Sci. Eng. A. 584 (2013) 21–31. https://doi.org/10.1016/j.msea.2013.06.055.

[66] H.D. Carlton, A. Haboub, G.F. Gallegos, D.Y. Parkinson, A.A. MacDowell, Damage evolution and failure mechanisms in additively manufactured stainless steel, Mater. Sci. Eng. A. 651 (2016) 406–414. https://doi.org/10.1016/j.msea.2015.10.073.

[67] A.A. Deev, P.A. Kuznetcov, S.N. Petrov, Anisotropy of mechanical properties and its correlation with the structure of the stainless steel 316L produced by the SLM method, Phys. Procedia. 83 (2016) 789–796. https://doi.org/10.1016/j.phpro.2016.08.081.

[68] T.M. Mower, M.J. Long, Mechanical behavior of additive manufactured, powder-bed laser-fused materials, Mater. Sci. Eng. A. 651 (2016) 198–213. https://doi.org/10.1016/j.msea.2015.10.068.

[69] J. Suryawanshi, K.G. Prashanth, U. Ramamurty, Mechanical behavior of selective laser melted 316L stainless steel, Mater. Sci. Eng. A. 696 (2017) 113–121. https://doi.org/10.1016/j.msea.2017.04.058.

[70] E. Garlea, H. Choo, C.C. Sluss, M.R. Koehler, R.L. Bridges, X. Xiao, Y. Ren, B.H. Jared, Variation of elastic mechanical properties with texture, porosity, and defect characteristics in laser powder bed fusion 316L stainless steel, Mater. Sci. Eng. A. 763 (2019) 138032. https://doi.org/10.1016/j.msea.2019.138032.

[71] C. Ni, Y. Shi, J. Liu, Influences of tilt angles on microstructure and mechanical properties of 316L stainless steel parts fabricated by selective laser melting (SLM), Mater. Res. Express. 6 (2019). https://doi.org/10.1088/2053-1591/ab2302.

[72] K. Chadha, Y. Tian, J.G. Spray, C. Aranas, Effect of annealing heat treatment on the microstructural evolution and mechanical properties of hot isostatic pressed 316L stainless steel fabricated by laser powder bed fusion, Metals (Basel). 10 (2020) 1–18. https://doi.org/10.3390/met10060753.

[73] A. Chniouel, P.F. Giroux, F. Lomello, P. Aubry, É. Vasquez, O. Hercher, H. Maskrot, Influence of substrate temperature on microstructural and mechanical properties of 316L stainless steel consolidated by laser powder bed fusion, Int. J. Adv. Manuf. Technol. 111 (2020) 3489–3503. https://doi.org/10.1007/s00170-020-06316-4.

[74] J. Kluczyński, L. Sniezek, K. Grzelak, J. Janiszewski, P. Płatek, J. Torzewski, I. Szachogłuchowicz, K. Gocman, Influence of selective laser melting technological parameters on the mechanical properties of additively manufactured elements using 316L austenitic steel, Materials (Basel). 13 (2020). https://doi.org/10.3390/ma13061449.

[75] Q. Portella, M. Chemkhi, D. Retraint, Influence of Surface Mechanical Attrition Treatment (SMAT) post-treatment on microstructural, mechanical and tensile behaviour of additive manufactured AISI 316L, Mater. Charact. 167 (2020). https://doi.org/10.1016/j.matchar.2020.110463.

[76] W.S. Shin, B. Son, W. Song, H. Sohn, H. Jang, Y.J. Kim, C. Park, Heat treatment effect on the microstructure, mechanical properties, and wear behaviors of stainless steel 316L prepared via selective laser melting, Mater. Sci. Eng. A. 806 (2021) 140805. https://doi.org/10.1016/j.msea.2021.140805.

[77] D. Kong, C. Dong, X. Ni, L. Zhang, J. Yao, C. Man, X. Cheng, K. Xiao, X. Li, Mechanical properties and corrosion behavior of selective laser melted 316L stainless steel after different heat treatment processes, J. Mater. Sci. Technol. 35 (2019) 1499–1507. https://doi.org/10.1016/j.jmst.2019.03.003.

[78] Y. Song, Q. Sun, K. Guo, X. Wang, J. Liu, J. Sun, Effect of scanning strategies on the microstructure and mechanical behavior of 316L stainless steel fabricated by selective laser melting, Mater. Sci. Eng. A. 793 (2020) 139879. https://doi.org/10.1016/j.msea.2020.139879.

[79] A.B. Kale, P. Alluri, A.K. Singh, S.H. Choi, The deformation and fracture behavior of 316L SS fabricated by SLM under mini V-bending test, Int. J. Mech. Sci. 196 (2021) 106292. https://doi.org/10.1016/j.ijmecsci.2021.106292.

[80] S. Dryepondt, P. Nandwana, P. Fernandez-Zelaia, F. List, Microstructure and high temperature tensile properties of 316L fabricated by laser powder-bed fusion, Addit. Manuf. 37 (2021) 101723. https://doi.org/10.1016/j.addma.2020.101723.

[81] A.D. Murphy-leonard, D.C. Pagan, P.G. Callahan, Z.K. Heinkel, C.E. Jasien, D.J. Rowenhorst, Materials Science & Engineering A Investigation of porosity , texture , and deformation behavior using high energy X-rays during in-situ tensile loading in additively manufactured 316L stainless steel, Mater. Sci. Eng. A. 810 (2021) 141034. https://doi.org/10.1016/j.msea.2021.141034.

[82] B. Barkia, P. Aubry, P. Haghi-Ashtiani, T. Auger, L. Gosmain, F. Schuster, H. Maskrot, On the origin of the high tensile strength and ductility of additively manufactured 316L stainless steel: Multiscale investigation, J. Mater. Sci. Technol. 41 (2020) 209–218. https://doi.org/10.1016/j.jmst.2019.09.017.

[83] S. Yin, X. Yan, R. Jenkins, C. Chen, M. Kazasidis, M. Liu, M. Kuang, R. Lupoi, Hybrid additive manufacture of 316L stainless steel with cold spray and selective laser melting: Microstructure and mechanical properties, J. Mater. Process. Technol. 273 (2019) 116248. https://doi.org/10.1016/j.jmatprotec.2019.05.029.

[84] T. Larimian, M. Kannan, D. Grzesiak, B. AlMangour, T. Borkar, Effect of energy density and scanning strategy on densification, microstructure and mechanical properties of 316L stainless steel processed via selective laser melting, Mater. Sci. Eng. A. 770 (2020) 138455. https://doi.org/10.1016/j.msea.2019.138455.

[85] K. Zhu, X. Chen, G.Q. Ding, J.L. Sun, Research on the Roughness Detection of Hot-Rolled Steel, in: IOP Conf. Ser. Mater. Sci. Eng., IOP Publishing, 2018: p. 22003.

[86] E. Yasa, J.P. Kruth, Microstructural investigation of selective laser melting 316L stainless steel parts exposed to laser re-melting, Procedia Eng. 19 (2011) 389–395. https://doi.org/10.1016/j.proeng.2011.11.130.

[87] K. Alrbaey, D. Wimpenny, R. Tosi, W. Manning, A. Moroz, On optimization of surface roughness of selective laser melted stainless steel parts: A statistical study, J. Mater. Eng. Perform. 23 (2014) 2139–2148. https://doi.org/10.1007/s11665-014-0993-9.

[88] D. Wang, Y. Liu, Y. Yang, D. Xiao, Theoretical and experimental study on surface roughness of 316L stainless steel metal parts obtained through selective laser melting, Rapid Prototyp. J. 22 (2016) 706–716. https://doi.org/10.1108/RPJ-06-2015-0078.

[89] K. Alrbaey, D.I. Wimpenny, A.A. Al-Barzinjy, A. Moroz, Electropolishing of Re-melted SLM

Stainless Steel 316L Parts Using Deep Eutectic Solvents: 3 × 3 Full Factorial Design, J. Mater. Eng. Perform. 25 (2016) 2836–2846. https://doi.org/10.1007/s11665-016-2140-2.

[90] Y. Sun, R. Bailey, A. Moroz, Surface finish and properties enhancement of selective laser melted 316L stainless steel by surface mechanical attrition treatment, Surf. Coat. Technol. 378 (2019) 124993.

[91] J. Zhang, A. Chaudhari, H. Wang, Surface quality and material removal in magnetic abrasive finishing of selective laser melted 316L stainless steel, J. Manuf. Process. 45 (2019) 710–719. https://doi.org/10.1016/j.jmapro.2019.07.044.

[92] Y. Bai, C. Zhao, J. Yang, J.Y.H. Fuh, W.F. Lu, C. Weng, H. Wang, Dry mechanical-electrochemical polishing of selective laser melted 316L stainless steel, Mater. Des. 193 (2020) 108840. https://doi.org/10.1016/j.matdes.2020.108840.

[93] S. Greco, S. Kieren-Ehses, B. Kirsch, J.C. Aurich, Micro milling of additively manufactured AISI 316L: impact of the layerwise microstructure on the process results, Int. J. Adv. Manuf. Technol. 112 (2021) 361–373. https://doi.org/10.1007/s00170-020-06387-3.

[94] J. Ghorbani, J. Li, A.K. Srivastava, Application of optimized laser surface re-melting process on selective laser melted 316L stainless steel inclined parts, J. Manuf. Process. 56 (2020) 726–734. https://doi.org/10.1016/j.jmapro.2020.05.025.

[95] E. Yasa, J. Deckers, J.P. Kruth, The investigation of the influence of laser re-melting on density, surface quality and microstructure of selective laser melting parts, Rapid Prototyp. J. 17 (2011) 312–327. https://doi.org/10.1108/13552541111156450.

[96] D. Wang, S. Mai, D. Xiao, Y. Yang, Surface quality of the curved overhanging structure manufactured from 316-L stainless steel by SLM, Int. J. Adv. Manuf. Technol. 86 (2016) 781–792. https://doi.org/10.1007/s00170-015-8216-6.

[97] Mid-Size Metal 3D Printer for all kind of materials, (n.d.). https://www.eos.info/en/additive-manufacturing/3d-printing-metal/eos-metal-systems/eos-m-290 (accessed September 28, 2021).

[98] Qual é il Costo dell'Energia Elettrica al kWh per le Aziende?, (n.d.). https://luce-gas.it/business/offerte/costo-kwh-aziende (accessed September 28, 2021).

[99] Home - Air Liquide Italia, (n.d.). https://industria.airliquide.it/ (accessed September 28, 2021).

[100] EOS StainlessSteel 316L Material Data Sheet Metal Solutions, (n.d.).

[101] Polveri ferrose, polveri non ferrose, graniglie di acciaio inox e speciali. | Pometon, (n.d.). https://www.pometon.com/it/ (accessed September 28, 2021).

[102] Mlab cusing R - Reactive Material DMLM Machine | GE Additive, (n.d.). https://www.ge.com/additive/additive-manufacturing/machines/dmlm-machines/mlab-r (accessed September 30, 2021).

[103] RTP80 - Sm Instruments, (n.d.). http://www.sm-instruments.com/it/prodotti/rugosimetri/rtp-80.html (accessed September 30, 2021).

[104] J. Zhang, A. Chaudhari, H. Wang, Surface quality and material removal in magnetic abrasive finishing of selective laser melted 316L stainless steel, J. Manuf. Process. 45 (2019) 710–719.

[105] H.C. Tran, Y.L. Lo, Systematic approach for determining optimal processing parameters to produce parts with high density in selective laser melting process, Int. J. Adv. Manuf. Technol. 105 (2019) 4443–4460. https://doi.org/10.1007/s00170-019-04517-0.

[106] K. Mumtaz, N. Hopkinson, Selective laser melting of Inconel 625 using pulse shaping, Rapid Prototyp. J. 16 (2010) 248–257.

8. List of Acronyms

LPBF	Laser Powder Bed Fusion
AM	Additive Manufacturing
CAD	Computer Aided Design
PBF	Powder Bed Fusion
DED	Directed Energy Deposition
EBM	Electron Beam Melting
SLM	Selective Laser Melting
LC	Laser Cusing
DMLS	Direct Metal Laser Sintering
WA	Water Atomizing (or Water Atomized)
GA	Gas Atomizing (or Gas Atomized)
PA	Plasma Atomizing (or Plasma Atomized)
VED	Volumetric Energy Density
XRD	X-Ray Diffraction
YS	Yield Strength
UTS	Ultimate Tensile Strength
SEM	Scanning Electron Microscope
DoE	Design of Experiment

9. List of Symbols

Symbol	Meaning	Unit of measure
VED	Volumetric energy density	J/mm^3
P	Laser power	W
Lt	Layer thickness	µm
Hs	Hatch spacing	µm
υ	Scanning speed	mm/s
E	Young modulus	GPa
YS	Yield strength	MPa
UTS	Ultimate tensile strength	MPa
ε_f	Elongation at failure	%
YS_0	Frictional stress in absence of grain boundaries	MPa
k	Constant of material	$\mu m^{0.5}$
d	Grain size	µm
C_j	Machine cost component	€/hour
M_p	Machine price	€
L_s	Machine lifespan	year
H_y	Yearly hours of use	hour/year
G_f	Gas flow	m^3/hour
G_p	Gas price	€/m^3
P_u	Power consumption	kW
P_c	Power cost	€/kWh
C_m	Material cost component	€/hour
V	Volume	mm^3
ρ	Density	kg/m3
p	Powder cost	€/kg
k_s	Support factor	
k_r	Recycle factor	
B_r	Build rate	mm/hour
H	Component height	mm

R_t	Recoating time	s
m_{dry}	Weight of sample	g
m_{dip}	Weight of sample dipped in water	g
ε	Elongation at maximum stress	%

Appendix I

In the Table below the density measurements are reported.

$$\rho_{Archimedes} = \frac{m_{dry} \cdot \rho_{H_2O}}{m_{dry} - m_{dip}}$$

$$Relative\ Density = \frac{\rho_{Archimedes}}{\rho_{316L\ theoretical}}$$

Where $\rho_{H_2O} = 0.997$ g/cm^3 and $\rho_{316L\ theoretical} = 7.99$ g/cm^3

Sample	m_{dry} (g)			Average m_{dry} (g)	m_{dip} (g)			Average m_{dip} (g)
	1	2	3		1	2	3	
GA01	13.1788	13.1778	13.1776	13.1781	11.5225	11.5215	11.5279	11.5240
GA02	13.3104	13.3108	13.3098	13.3103	11.638	11.6365	11.6384	11.6376
GA03	13.305	13.3045	13.3043	13.3046	11.6215	11.6231	11.6238	11.6228
GA04	13.1662	13.1659	13.166	13.1660	11.467	11.4661	11.4666	11.4666
GA05	13.1021	13.1023	13.1019	13.1021	11.4586	11.4556	11.4575	11.4572
GA06	13.2286	13.2283	13.2284	13.2284	11.5624	11.5651	11.5703	11.5659
GA07	13.2738	13.2736	13.2739	13.2738	11.5957	11.5998	11.5962	11.5972
GA08	13.0542	13.0544	13.0541	13.0542	11.366	11.3664	11.3652	11.3659
GA09	12.9966	12.9963	12.9964	12.9964	11.3666	11.366	11.3662	11.3663
GA10	13.1679	13.1675	13.1673	13.1676	11.5141	11.5144	11.5155	11.5147
GA11	13.2077	13.2075	13.2074	13.2075	11.5444	11.5451	11.5453	11.5449
GA12	13.1365	13.1363	13.1359	13.1362	11.4564	11.4577	11.457	11.4570
GA13	12.9111	12.9108	12.911	12.9110	11.2928	11.2932	11.2907	11.2922
GA14	13.0623	13.0628	13.0626	13.0626	11.4275	11.4256	11.4264	11.4265
GA15	13.0934	13.0933	13.0931	13.0933	11.4503	11.4502	11.4511	11.4505
GA16	13.0757	13.0758	13.0755	13.0757	11.4077	11.4081	11.4098	11.4085
WA01	10.7675	10.7676	10.7672	10.7674	9.3851	9.3845	9.3847	9.3848
WA02	10.946	10.9462	10.9463	10.9462	9.5458	9.5491	9.5474	9.5474
WA03	10.9612	10.9614	10.9611	10.9612	9.5521	9.5516	9.5528	9.5522
WA04	10.9249	10.9251	10.9254	10.9251	9.5067	9.5079	9.5062	9.5069
WA05	10.6181	10.6182	10.6184	10.6182	9.2468	9.2462	9.2476	9.2469
WA06	10.8107	10.8108	10.8103	10.8106	9.4361	9.4336	9.4373	9.4357
WA07	10.9478	10.9474	10.9477	10.9476	9.5557	9.5547	9.5564	9.5556
WA08	10.7109	10.712	10.7119	10.7116	9.3142	9.3126	9.3157	9.3142
WA09	10.6186	10.6184	10.6191	10.6187	9.2791	9.2824	9.2802	9.2806
WA10	10.8957	10.896	10.8958	10.8958	9.5128	9.5139	9.5136	9.5134
WA11	10.9411	10.9413	10.941	10.9411	9.5453	9.5475	9.5451	9.5460
WA12	10.9222	10.9227	10.9223	10.9224	9.5198	9.5205	9.5194	9.5199
WA13	10.4449	10.4446	10.4451	10.4449	9.0908	9.0912	9.0922	9.0914
WA14	10.6528	10.6527	10.6531	10.6529	9.2835	9.2843	9.2848	9.2842

WA15	10.8512	10.8522	10.8523	10.8519	9.4707	9.4715	9.4728	9.4717
WA16	10.6814	10.6821	10.6808	10.6814	9.3154	9.3163	9.315	9.3156

Sample	Archimede density (g/cm3)	Relative density (%)
GA01	7.9430	99.41
GA02	7.9335	99.29
GA03	7.8872	98.71
GA04	7.7239	96.67
GA05	7.9416	99.39
GA06	7.9331	99.29
GA07	7.8936	98.79
GA08	7.7087	96.48
GA09	7.9485	99.48
GA10	7.9424	99.40
GA11	7.9201	99.12
GA12	7.7994	97.62
GA13	7.9520	99.52
GA14	7.9602	99.63
GA15	7.9465	99.46
GA16	7.8197	97.87
WA01	7.7641	97.17
WA02	7.8023	97.65
WA03	7.7557	97.07
WA04	7.6804	96.13
WA05	7.7196	96.62
WA06	7.8390	98.11
WA07	7.8409	98.13
WA08	7.6422	95.65
WA09	7.9117	99.02
WA10	7.8582	98.35
WA11	7.8186	97.86
WA12	7.7644	97.18
WA13	7.6940	96.29
WA14	7.7600	97.12
WA15	7.8388	98.11
WA16	7.7968	97.58

Appendix II

Surface roughness measurements.

Sample	Ra (µm)				
	Top surface	Lateral1	Lateral2	Lateral3	Lateral4
GA01	9.933	3.750	3.450	3.827	5.228
GA02	9.872	4.221	4.913	4.900	5.287
GA03	12.228	4.247	4.613	4.868	4.193
GA04	11.570	5.103	6.096	5.665	5.271
GA05	9.928	4.037	4.093	3.814	4.609
GA06	7.889	3.624	4.099	4.891	3.939
GA07	11.957	4.487	4.743	4.392	4.690
GA08	14.427	5.453	5.262	5.543	5.288
GA09	8.573	4.111	5.076	4.346	3.985
GA10	8.963	4.089	4.809	4.896	3.903
GA11	12.012	4.807	5.390	5.368	4.046
GA12	13.558	5.202	5.130	5.124	5.726
GA13	10.763	4.609	4.855	7.173	6.749
GA14	8.391	4.339	5.221	3.807	3.795
GA15	11.311	4.494	5.295	4.135	5.259
GA16	10.272	5.236	6.469	4.831	4.713
WA01	15.028	3.726	3.313	3.564	3.949
WA02	10.913	3.192	3.262	4.361	4.416
WA03	10.836	3.308	4.012	5.007	4.410
WA04	11.474	5.049	4.377	5.258	4.786
WA05	16.930	4.028	3.248	3.730	4.191
WA06	13.373	3.031	4.032	3.954	3.516
WA07	12.355	3.282	4.201	4.689	4.261
WA08	11.952	4.217	4.863	3.796	4.626
WA09	14.982	3.645	4.198	3.482	3.604
WA10	13.589	3.706	4.096	4.085	3.679
WA11	13.011	3.052	3.919	3.803	3.920
WA12	10.587	4.813	4.570	4.393	4.323
WA13	15.461	4.335	4.581	3.521	3.801
WA14	14.605	3.568	4.150	3.879	3.790
WA15	10.787	4.397	3.618	4.090	3.747
WA16	12.369	4.831	4.734	4.994	2.854

Sample	Rz (µm)				
	Top surface	Lateral1	Lateral2	Lateral3	Lateral4
GA01	49.340	24.518	26.114	26.298	35.011
GA02	51.805	28.385	34.168	31.915	34.526
GA03	60.724	29.250	32.730	30.147	29.512
GA04	62.268	34.496	36.818	35.788	34.845
GA05	48.422	28.108	25.980	24.955	30.353
GA06	42.561	24.788	29.092	31.933	25.811
GA07	59.606	31.393	30.564	29.422	31.257
GA08	75.976	34.164	35.692	31.797	35.627
GA09	49.029	28.718	31.933	29.146	27.558
GA10	48.327	27.246	34.222	31.154	24.923
GA11	64.188	30.544	34.883	34.331	29.143
GA12	69.683	33.581	31.079	33.000	37.626
GA13	58.197	29.369	30.276	43.275	39.122
GA14	43.754	27.218	31.665	25.905	23.628
GA15	56.173	28.614	35.232	26.141	34.181
GA16	56.353	31.348	39.837	30.952	33.723
WA01	73.635	23.412	23.281	24.920	27.632
WA02	57.623	25.275	24.177	30.885	30.166
WA03	55.811	26.400	26.925	31.454	29.247
WA04	61.263	32.475	28.372	30.060	31.995
WA05	81.001	26.805	22.916	23.801	29.246
WA06	64.003	22.993	27.872	27.924	26.698
WA07	64.761	27.374	29.685	31.433	26.921
WA08	58.348	30.368	33.948	28.560	30.057
WA09	69.918	25.362	28.408	24.124	30.324
WA10	68.435	30.140	26.696	26.461	28.087
WA11	66.288	23.199	30.315	24.575	26.450
WA12	54.397	31.665	31.430	31.580	31.764
WA13	77.943	29.524	30.262	24.776	25.484
WA14	71.657	25.839	27.099	26.597	27.106
WA15	55.458	28.756	24.325	28.543	28.915
WA16	63.040	30.854	28.985	33.755	20.030

Appendix III

Stress-strain graphs of tensile samples.

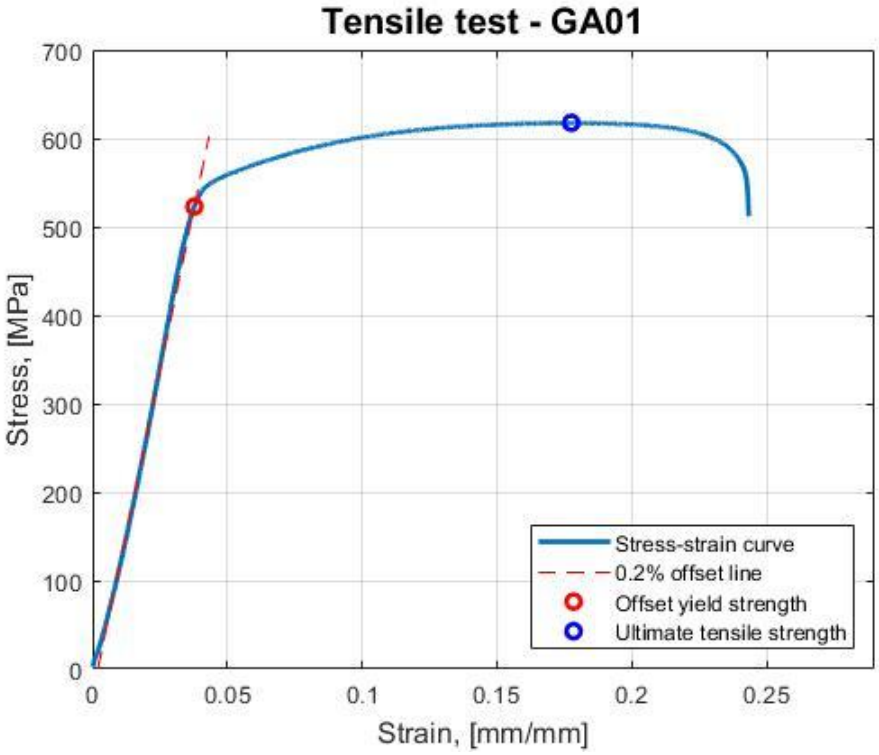

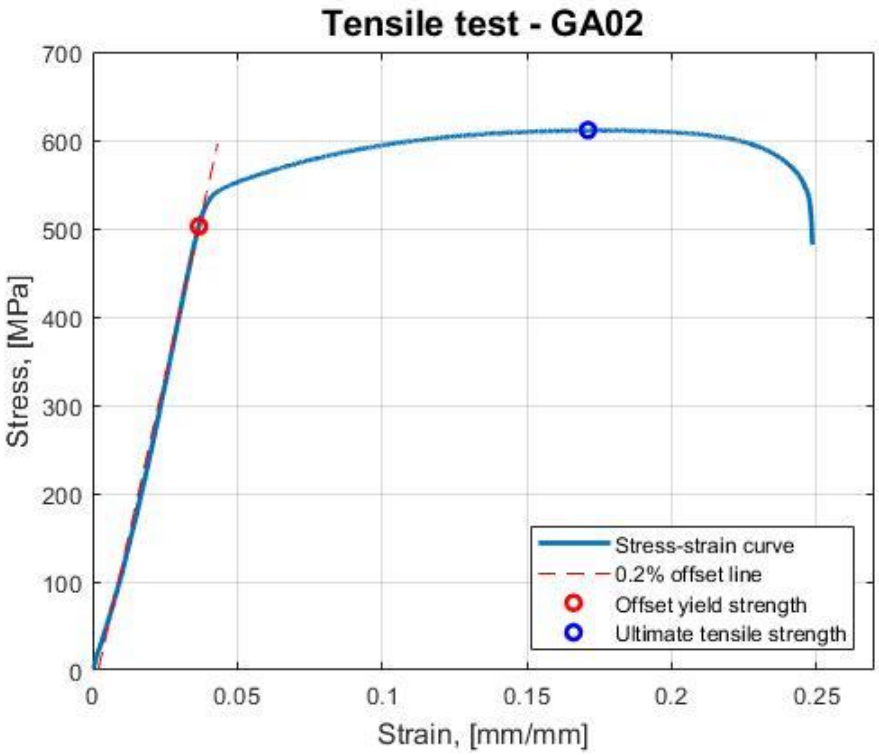

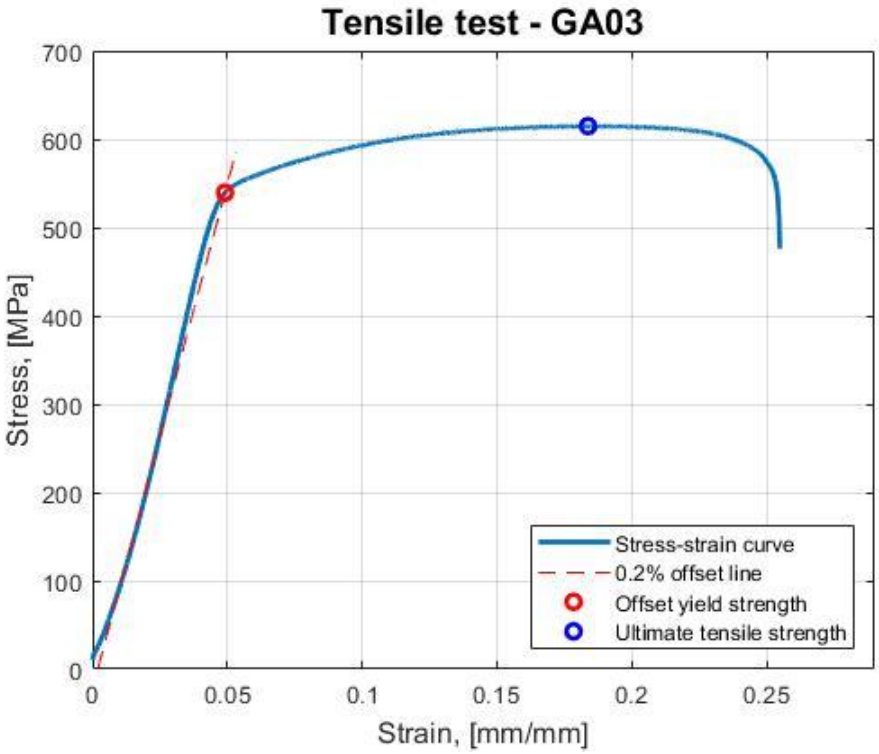
Tensile test - GA03
Stress, [MPa]
Strain, [mm/mm]
Stress-strain curve
0.2% offset line
Offset yield strength
Ultimate tensile strength

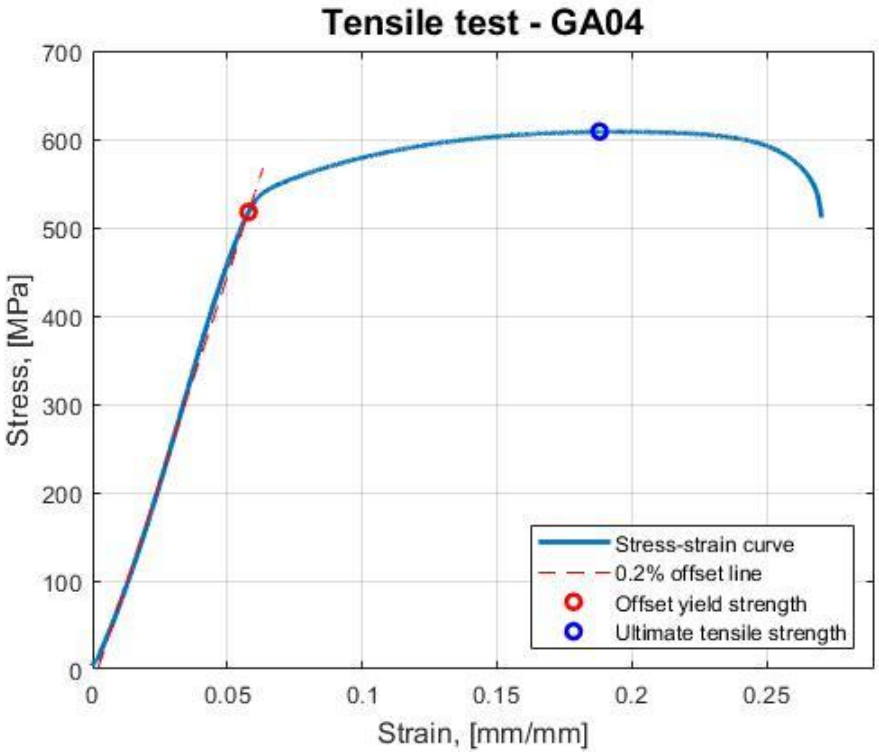
Tensile test - GA04
Stress, [MPa]
Strain, [mm/mm]
Stress-strain curve
0.2% offset line
Offset yield strength
Ultimate tensile strength

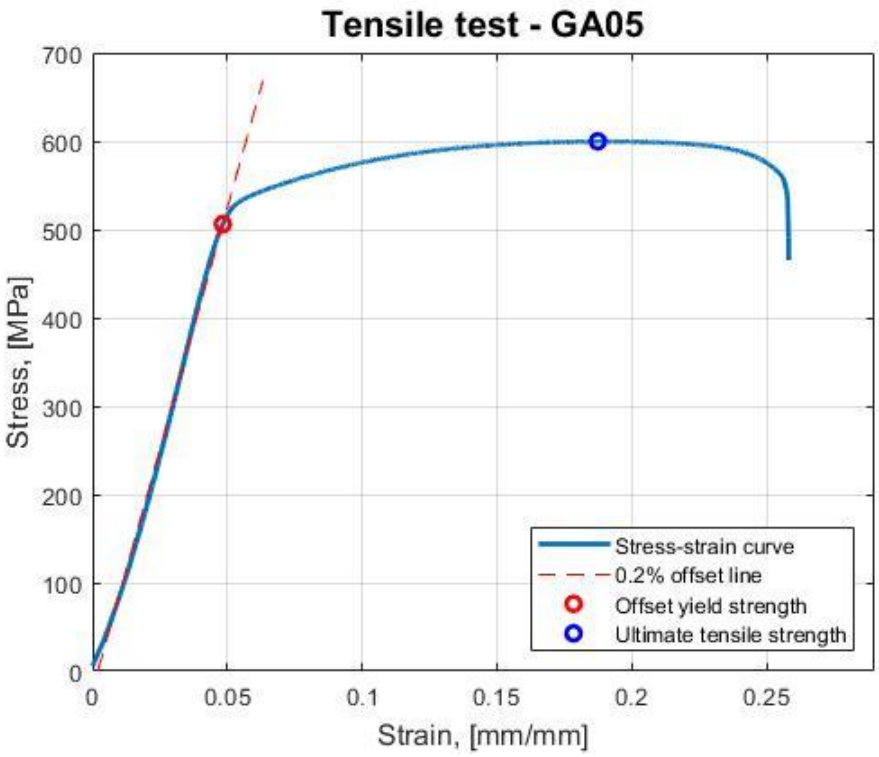
Tensile test - GA05
Stress, [MPa]
Strain, [mm/mm]
Stress-strain curve
0.2% offset line
Offset yield strength
Ultimate tensile strength

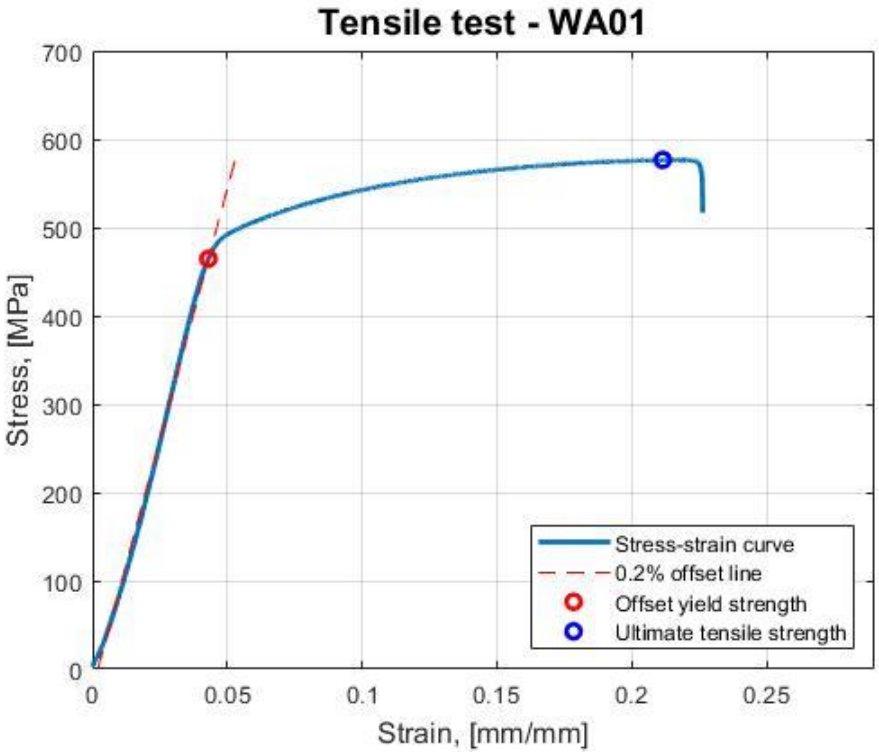
Tensile test - WA01
Stress, [MPa]
Strain, [mm/mm]
Stress-strain curve
0.2% offset line
Offset yield strength
Ultimate tensile strength

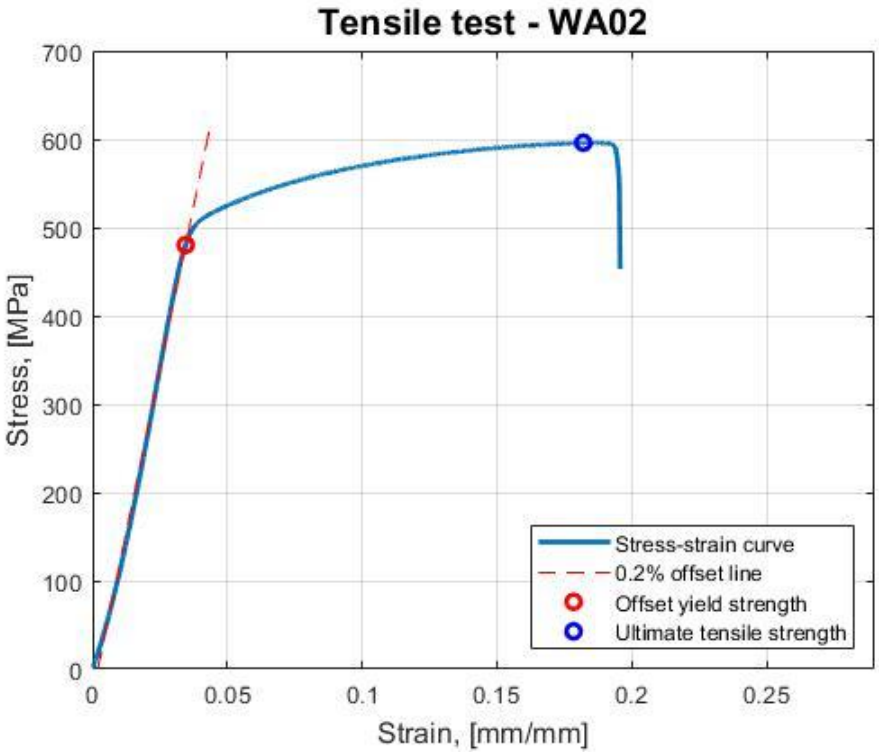
Tensile test - WA02
Stress, [MPa]
Strain, [mm/mm]
Stress-strain curve
0.2% offset line
Offset yield strength
Ultimate tensile strength

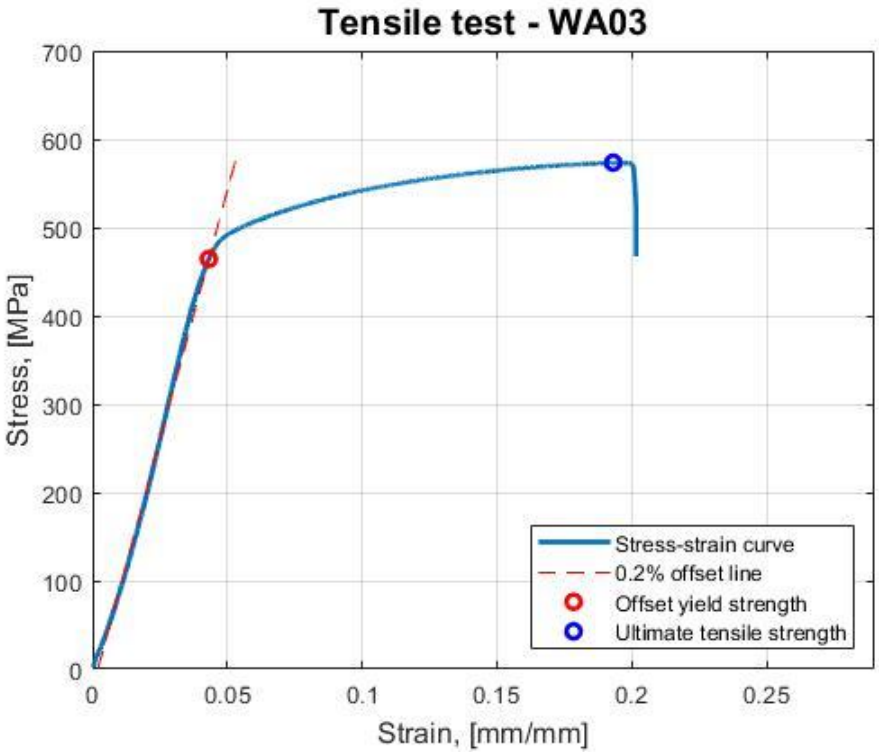
Tensile test - WA03
Stress, [MPa]
Strain, [mm/mm]
Stress-strain curve
0.2% offset line
Offset yield strength
Ultimate tensile strength